PATH INTEGRAL METHODS USING FEYNMAN-KAC FORMULA AND REFLECTING BROWNIAN MOTIONS FOR NEUMANN AND ROBIN PROBLEMS

by

Yijing Zhou

A dissertation submitted to the faculty of
The University of North Carolina at Charlotte
in partial fulfillment of the requirements
for the degree of Doctor of Philosophy in
Applied Mathematics

Charlotte

2016

Approved by:

_____

Dr. Wei Cai

_____

Dr. Duan Chen

_____

Dr. Shaozhong Deng

_____

Dr. Greg Gbur

ABSTRACT

YIJING ZHOU. Path integral methods using Feynman-Kac formula and reflecting Brownian motions for Neumann and Robin Problems. (Under the direction of DR. WEI CAI)

In this dissertation, we propose numerical methods for computing the boundary local time of reflecting Brownian motion (RBM) in R^3 and its use in the probabilistic representation of the solution of the Laplace equation with the Neumann and Robin boundary conditions respectively. Approximations of RBM based on a walk-on-spheres (WOS) and random walk on lattices are discussed and tested for sampling RBM paths and their applicability in finding accurate approximation of the local time and discretization of the probabilistic formula. Numerical tests for a cube domain have shown the convergence of the numerical methods as the time length of RBM paths and number of paths sampled increases. Spherical, ellipsoidal, noconvex domains were also tested to prove the efficiency and accuracy of the algorithm. Moreover, an exterior Neumann problem of a many-spheres system further demonstrated the effectiveness of the method even the starting point of the path lying exactly on the boundary. Additionally, the application in electrical impedance tomography to solve the forward problem further demonstrates the simplicity and efficiency of our approach, which is extremely important for some reconstruction methods of the inverse problem. Other applications in material science in calculating the electrical properties of materials in special shapes are also discussed as possible future work.

ACKNOWLEDGMENTS

The study was carried out in the Department of Mathematics and Statistics during 2012-2016. The study was supported by the National Science Foundation and the National Science Foundation of China.

I wish to express my greatest gratitude to my dissertation advisor, Professor Wei Cai. Without his continuous encouragement and guidance, it is impossible for me to complete this dissertation. His honest and patience impressed me and encouraged me to pursue the beauty of mathematics – simplicity. His advice constantly inspired me and thus numerous improvement can be achieved. To Professor Joel Avrin and Shaozhong Deng, I express my appreciation for their efforts as the graduate coordinators. Their pertinent suggestions on my personal study plan enable me to finish the graduate study. I also thank Professor Duan Chen and Greg Gbur who are willing to be part of the dissertation committee and always ready for help. I thank Dr. Jack F. Douglas for providing ZENO software and insightful suggestions on distance calculation in special geometry structures.

I wish to thank Professor Changhao Yan, who offered and shared programming resources with me so that I am able to start and be proficient in programming later on.

I offer my thanks to everyone in Professor Wei Cai's group. The weekly discussions on the researches helped me gain a great perspective on different areas and topics.

I devote my dissertation to family, Liqin Su and Daniel Su, for your constant love and care.

TABLE OF CONTENTS

LIST OF FIGURES

LIST OF TABLES

CHAPTER 1: INTRODUCTION

The thesis focuses on the simulation of standard reflecting Brownian motion and numerical realization of the well known Feynman-Kac formula [14] for the Laplace operator given the Neumann and/or Robin boundary conditions in a bounded domain. Different from the conventional numerical methods, like finite element, finite difference and boundary element methods, Feynman-Kac formula successfully connects the solutions of differential equations of diffusion and heat flow and random processes of Brownian motions, which provides an alternative way to solve PDEs without constructing spatial mesh.

The Feynman-Kac formula represents the solutions of parabolic and elliptic PDEs as the expectation functionals of stochastic processes (specifically Brownian motions), and conversely, the probabilistic properties of diffusion processes can be obtained through investigating related PDEs characterized by corresponding generators [43]. The formula involves the path integrals of the diffusion process starting from an arbitrarily prescribed location, and this enables us to find a local numerical solution without constructing space and time meshes as in traditional deterministic numerical methods mentioned above, which incur expensive costs in high dimensions. In many applications it is also of practical importance and necessity to seek a local solution of PDEs at some interested points. If the sample paths of a diffusion process are simulated, then by computing the average of path integrals we can obtain approximations to the exact solutions of the PDEs. For second order elliptic PDEs with Dirichlet and Neumann boundaries, the average of path integrals is reduced

to the average of boundary integrals under certain measure where the detailed trajectories of the diffusion process have no effect on the averages except the hitting locations on the boundaries.

In the Dirichlet case, the underlying stochastic process is Brownian motion and its path will terminate upon reaching the boundary, also called killed Brownian motion. For the Neumann and/or Robin boundary conditions, the reflecting Brownian motion comes into play instead which will have instantaneous reflection on the boundary.

Simulations of diffusion paths can be done by random walks methods [27] [2][35][20] either on lattice or in continuum space. In some cases such as for the Poisson equation, the Feynman-Kac formula has a pathwise integral requiring the detailed trajectory of each path. Moreover, one may need to adopt random walks on a discrete lattice in order to incorporate inhomogeneous source terms. As for the continuum space approach, the Walk on Spheres (WOS) method is preferred where the path of diffusion process within the domain does not appear in the Feynman-Kac formula. For Laplace equation, Walk on Spheres method turns out to be more efficient and effortless when the dimensions are high.

Chapter 2 is prepartory. We introduce the basic concepts of reflecting Brownian motion and its boundary local time which arised from the Skorohod problem in a bounded domain. In Chapter 3, the boundary value problems associated with laplace equation are discussed and we give the explicit form of the probabilistic solutions. The Walk-on-Spheres method is described in Chapter 4 in details and based on which the numerical methods and results of the boundary value problems are given in Chapter 5. In Chapter 6, the forward problem in electric impedance tomography is treated on the basis of a Robin-to-Neumann mapping using generalized Feynman-Kac formula. Numerical results are given to a unit sphere in

three dimensions.

CHAPTER 2: REFLECTING BROWNIAN MOTION, BOUNDARY LOCAL TIME AND SKOROHOD PROBLEM

2.1 Reflecting Brownian Motion

2.1.1 Brownian Motion

Let us review the definition of Brownian motion first. Mathematically, the transition density function $\widetilde{p}(t,x,y)$ of Brownian motion process satisfies the following parabolic differential equation:

$$\begin{cases} \dfrac{\partial}{\partial t}\widetilde{p}(t,x,y) = \dfrac{1}{2}\Delta_x \widetilde{p}(t,x,y), \quad (t,x,y) \in R^+ \times R^d \times R^d; \\ \lim\limits_{t\to 0}\widetilde{p}(t,x,y) = \delta_y(x), \quad (x,y) \in R^d \times R^d. \end{cases} \tag{2.1.1}$$

The first equation in $(2.1.1)$ is known as the heat equation. It is motivated by the diffusion of heat through space (e.g. a steel rod). From the PDE theory, the heat equation has fundamental solution in one dimension

$$\widetilde{p}(t,x) = \frac{1}{\sqrt{2\pi t}} e^{-x^2/2t}, \tag{2.1.2}$$

which is exactly the density function of Brownian motion.

The $\widetilde{p}(t,x,y)$ above describes the microscopic movement of a Brownian particle throughout the whole space. Next, a formal mathematical definition presents the general features of Brownian motion.

Definition 1. Brownian motion: A Brownian motion $B(t) = (B_1(t), B_2(t), ..., B_d(t))$ in R^d

is a set of d independent stochastic processes with the following properties: for $1 \leq i \leq d$,

1. (Normal increments) $B_i(t) - B_i(s)$ has the normal distribution with mean 0 and variance $t - s$.

2. (Independence of increments) $B_i(t) - B_i(s)$ is independent of the past, i.e., of B_u, $0 \leq u \leq s$.

3. (Continuity of paths) $B_i(t), t \geq 0$ is a continuous function of t.

Another important fact is that every Brownian sample path is a nowhere differentiable function of t.

2.1.2 Reflecting Brownian Motion

As shown in (2.1.1), Brownian motion is defined in the whole space while reflecting Brownian motion (RBM) only exists within a bounded domain with certain constraints. Similarly, the transition density function $p(t,x,y)$ of RBM satisfies a modified boundary value problem with an additional boundary condition in a bounded $D \in R^d$:

$$\begin{cases} \dfrac{\partial}{\partial t} p(t,x,y) = \dfrac{1}{2}\Delta_x p(t,x,y), \quad (t,x,y) \in R^+ \times D \times D; \\ \lim\limits_{t \to 0} p(t,x,y) = \delta_y(x), \quad (x,y) \in \bar{D} \times \bar{D}; \\ \dfrac{\partial}{\partial n_x} p(t,x,y) = 0, \quad (t,x,y) \in R^+ \times \partial D \times D. \end{cases} \tag{2.1.3}$$

The normal derivative (2.1.3) being zero implies that the path of RBM will not be able to move out to the exterior of the domain but reflect back along the normal inwardly each time it reaches the boundary. Obviously, the path of RBM behaves like the Brownian motion in the interior of the domain but behave differently on the boundary.

The existence for the transition density function $p(t,x,y)$ is guaranteed by a C^3 boundary [14] and the function can be constructed by a well-known method in the theory of partial differential equations. Detailed proof is omitted here.

Next, we state some properties of $p(t,x,y)$ in a theorem.

Theorem 1. The function $p(t,x,y)$ in $(2.1.3)$ has the following properties:

1. $p(t,x,y) > 0$;

2. $p(t,x,y)$ is symmetric in x and y;

3.

$$\int_D p(t,x,y)\sigma(dy) = 1; \tag{2.1.4}$$

4. The Chapman-Kolmogoroff equation holds:

$$p(t+s,x,y) = \int_D p(t,x,z)p(s,z,y)\sigma(dz); \tag{2.1.5}$$

Property 1 is a consequence of a strong version of the maximum principle. Property 2 is proved by using the self-ajointness of the Laplacian operator with the zero Neumann boundary condition. Property 3 and 4 are derived from the uniqueness of the solution of the first two equations of $(2.1.3)$. The four properties together ensure that $p(t,x,y)$ is the transition density function of a reflecting Brownian motion [14].

2.2 Skorohod Problem

2.2.1 One Dimensional Case

Let B_t denote a standard Brownian motion in R and any $x \in R$, then the positive submartingale $|B_t - x|$ is called the reflecting Brownian motion at x and it has the decomposition as the sum of another Brownian motion $\hat{B}_t$ and a continuous nondecreasing process

$L(t,x)$:

$$|B_t - x| = \hat{B}_t + L(t,x), \tag{2.2.1}$$

where $L(t,x)$ is the local time of B_t at x and was first proposed by P. Lévy [18]. It is defined as follows:

$$\begin{aligned} L(t,x) &= \lim_{\varepsilon \to 0} \frac{1}{2\varepsilon} \int_0^t I_{(x-\varepsilon, x+\varepsilon)}(B_s) ds \\ &= \lim_{\varepsilon \to 0} \frac{1}{2\varepsilon} m\{s \in [0,t] : B_x \in (x-\varepsilon, x+\varepsilon)\}. \end{aligned} \tag{2.2.2}$$

(2.2.1) is the Skorohod equation in one dimension and as a matter of fact, the Tanaka's formula gives the solution to it.

Tanaka's formula For each (t,x), we have a.s.

$$|B_t - x| = |B_0 - x| + \int_0^t sgn(B_s - x) dB_s + L(t,x), \tag{2.2.3}$$

and almost surely, $L(t,x)$ increases only when $|B_t - x|$ is at zero, i.e.,

$$\int_0^\infty 1_{\{t:B(t) \neq x\}} dL(t,x) = 0 \quad a.s.. \tag{2.2.4}$$

Further, by comparing (2.2.1) with (2.2.3), it reveals that

$$\hat{B}(t,x) = |B_0 - x| + \int_0^t sgn(B_s - x) dB_s. \tag{2.2.5}$$

This can be proved by calculating the quadratic variations of both sides of the equation [6].

Remark 1. Without loss of generality, by setting $x = 0$ in (2.2.3), we have

$$|B| = \hat{B} + L. \tag{2.2.6}$$

It can be proved that $|\hat{B}|$ is equivalent in law to $|B|$, but it is not possible that $|\hat{B}|$ is equal

to $|B|$. Otherwise, if $|\hat{B}| = |B|$, then (2.2.6) would be $|\hat{B}| = \hat{B} + L$ where $|\hat{B}|$ and $\hat{B}$ are simultaneously zero for a sequence of times approaching ∞, and this would lead to $L \equiv 0$ which is not true. Simply speaking, the equivalence in law of two processes will not imply the equality of sample paths.

It is interesting that $|B|$ is called the reflection of the Brownian motion B and $\hat{B}$ has the same distribution as B. This inspires us the idea of construction of sample path of $|B|$ from B directly. Details can be found in Chapter 5.

2.2.2 Generalized Skorohod equation

In this section, we give the formulaiton of Skorohod problem in multi-dimensional Euclidean space.

Definition 2. Skorohod equation: Assume D is a bounded domain in R^d with a C^2 boundary. Let $f(t)$ be a (continuous) path in R^d with $f(0) \in \bar{D}$. A pair (ξ_t, L_t) is a solution to the Skorohod equation $S(f;D)$ if the following conditions are satisfied:

1. ξ is a path in $\bar{D}$;

2. $L(t)$ is a nondecreasing function which increases only when $\xi \in \partial D$, namely,

$$L(t) = \int_0^t I_{\partial D}(\xi(s))L(ds); \tag{2.2.7}$$

3. The Skorohod equation holds:

$$S(f;D): \qquad \xi(t) = f(t) - \frac{1}{2}\int_0^t n(\xi(s))L(ds), \tag{2.2.8}$$

where $n(x)$ stands for the outward unit normal vector at $x \in \partial D$.

Remark 2. In Definition 2, the smoothness constraint on D can be relaxed to bounded domains with C^1 boundaries, which however will only guarantee the existence of $(2.2.8)$. But for a domain D with a C^2 boundary, the solution will be unique. Obviously, (ξ_t, L_t) is continuous in the sense that each component is continuous.

The Skorohod problem was first studied in [28] by A.V. Skorohod in addressing the construction of paths for diffusion processes with boundaries, which results from the instantaneous reflection behavior of the processes at the boundaries. Skorohod presented the result in one dimension in the form of an Ito integral and Hsu [14] later extended the concept to d-dimensions $(d \geq 2)$.

Theorem 2. Let D be a bounded domain in R^d with C^1 boundary and f be a continuous path in R^d wih $f(0) \in \bar{D}$. Then the solution to the Skorohod equation (2.2.8) exists and is unique if D has C^2 boundary.

The full proof was given in [14]. The existence of the solution was shown by explicit construction for the right continuous step path f in R^d and then generalized to any continuous path by taking the limit, which also guarantees the uniqueness according to the Arzelá-Ascoli theorem. Furthermore, the moduli fo continuity of ξ is no less continuous than f which can be observed by the construction of ξ from f. Besides, Theorem 2 is also true for unbounded domains.

Theorem 3. Suppose D is a bounded domain with C^3 boundary. Let B_t be standard Brownian motion starting at $x \in \overline{D}$. If X_t and L_t are continuous stochastic processes in R^d and R^+ respectively, such that with probability one, (X_t, L_t) is the solution to the Skorohod equation $S(B : D)$, then X_t has the law of SRBM in D.

The proof Theorem 3 is established by identifying the equivalence of the reflecting Brownian motion and the solution to the submartingale problem . Because the transition probability density of the SRBM satisfies the same parabolic differential equation as that by a BM, a sample path of the SRBM can be simulated simply as that of the BM within the domain. However, the zero Neumann boundary condition for the density of SRBM implies that the path be pushed back at the boundary along the inward normal direction whenever it attempts to cross the boundary. We shall see the construction of a SRBM from a SBM in latter chapters.

In the rest of the thesis, we only discuss the reflecting Brownian motion X_t and its local time $L(t)$.

2.3 Boundary Local Time

Now, we may want to further look into the local time $L(\cdot)$.

In (2.2.2), if we treat x as a boundary, then (2.2.7) is essentially the extention of (2.2.2) and it measures the amount of time ξ_t spend in the neighborhood of the boundary within the time period $[0,t]$. Therefore, we may call it bounary local time. It is the unique continuous nondecreasing process that appears in the Skorohod equation (2.2.8) [14] [19] [25]. In the measure theory, it is well established that $t \in R_+ : X_t \in \partial D$ is a closed set with Lebesgue measure zero while the sojourn tme of the set is nontrivial. In fact, it exists both in L^2 and a.s.. This concept provides a powerful tool in studying the Brownian sample paths. Moreover, it is not just a mathematical one but also has physical relevance in understanding the crossover exponent associated with renewal rate in modern renewal theory [12].

Theorem 4. Let D be a bounded domain with C^3 boundary, B_t be the standard Brownian

motion in R^d with starting point $x \in \overline{D}$ and (X_t, L_t) be the solution to the Skorohod equation $S(B : D)$. Then with probability one,

$$\lim_{\varepsilon \to 0} \int_0^t \frac{I_{D_\varepsilon}(X_s)}{\varepsilon} = L(t) \tag{2.3.1}$$

and in $L^2(P^x)$ for each fixed t. Here D_ε is a strip region of width ε containing ∂D and $D_\varepsilon \subset D$.

(2.3.1) may be utilized as the new definition of boundary local time. Next, Skorohod integral is introduced to give an explicit formula for boundary local time.

Theorem 5. The integral

$$\int_0^t I_{\partial D}\{X_s\} \sqrt{ds} \tag{2.3.2}$$

exists. Moreover, the boundary local time L_t of SRBM X_t can be expressed as

$$L(t) = \sqrt{\frac{\pi}{2}} \int_0^t I_{\partial D}\{X_s\} \sqrt{ds}, \tag{2.3.3}$$

where the right-hand side of (2.3.3) is understood as the limit of

$$\sum_{i=1}^{n-1} \max_{s \in \Delta_i} I_{\partial D}(X_s) \sqrt{|\Delta_i|}, \quad \max_i |\Delta_i| \to 0, \tag{2.3.4}$$

and $\Delta = \{\Delta_i\}$ is a partition of the interval $[0,t]$ and each Δ_i is an element in Δ.

Now we have three different forms of boundary local time L_t of reflecting Brownian motion, (2.2.7), (2.3.1) and (2.3.3). It can be shown that they are equivalent in probability and L^2. We will discuss the implementation of both (2.3.1) and (2.3.3) in Chapter 5.

CHAPTER 3: BOUNDARY VALUE PROBLEMS

In this chapter, we introduce the well-known Feynman-Kac formulas for boundary value problems associated with Schrödinger operator. The formulation is established on the expectation functionals of stochastic processes, specifically standard Brownian motion, under certain probability space. The generalizations are mainly focused on two types in financial applications: (a) those where other Ito diffusion processes and (b) those in which the diffusion process is confined in a region of space. In this chapter, we mainly discuss the latter case.

3.1 Review of Dirichlet Problem

Let us consider the following Dirichlet problem of general elliptic PDE in a bounded domain $D \subset R^d$.

$$\begin{cases} L(u) \equiv \sum_{i=1}^{n} b_i(x) \dfrac{\partial u}{\partial x_i} + \sum_{i,j=1}^{n} a_{ij}(x) \dfrac{\partial^2 u}{\partial x_i \partial x_j} = f(x),\ x \in D \\ \\ u = \phi_1(x),\ x \in \partial D \end{cases} \tag{3.1.1}$$

Let X_t be the Ito diffusion relating to the standard Brownian motion B_t,

$$dX_t = b(X_t)dt + \alpha(X_t)dB_t, \tag{3.1.2}$$

where $[a_{ij}] = \frac{1}{2}\alpha(x)\alpha^T(x)$, then Feynman-Kac formula provides a probabilistic solution [12] to (3.1.1) as

$$u(x) = E^{x_0}\left(\phi_1\left(X_{\tau_D}\right)\right) + E^{x_0}\left[\int_0^{\tau_D} f(X_t)dt\right]. \tag{3.1.3}$$

Here τ_D stands for the first hitting time of the domain boundary. The expectation in (3.1.3) calculates the expected value of functions in the probability space $P^x(D)$ of X_t with $X_0 = x_0$.

Note that when $b_i = 0$, $a_{ij} = 1$ and $f(x) = 0$, elliptic PDE (3.1.1) is reduced to the Poisson equation with no source term, or Laplace equation. Then (3.1.3) becomes

$$u(x) = E^{x_0}\left(\phi_1\left(X_{\tau_D}\right)\right), \tag{3.1.4}$$

which shows that u can be evaluated as an average of the boundary values at the first hitting positions on the boundary. Since X_t stops moving and begin absorbed once hits the boundary, one may call it *killed Brownian motion*.

3.2 Neumann Problem

Now consider the Neumann boundary value problem of the elliptic PDE on bounded doamin $D \subset R^d$,

$$\begin{cases} \left(\dfrac{\Delta}{2} + q(x)\right) u = 0,\ x \in D \\ \qquad\qquad \dfrac{\partial u}{\partial n} = \phi_2(x),\ x \in \partial D \end{cases} \tag{3.2.1}$$

When the bottom of the spectrum of the operator $\Delta/2 + q$ is negative a probablistic solution of (3.2.1) is given by

$$u(x) = \frac{1}{2} E^x \left[\int_0^\infty e_q(t)\phi_2(X_t)L(dt)\right], \tag{3.2.2}$$

where X_t is a SRBM starting at x, L_t is the boundary local time w.r.t. X_t and $e_q(t)$ is the Feynman-Kac functional [14]

$$e_q(t) = \exp\left[\int_0^t q(X_s)\,ds\right].$$

Remark 3. Comparing with formula (3.2.2), we find that the probabilistic solutions to

the Laplace equation with the Dirichlet boundary condition has a very similar form (see (3.1.4)). In the Dirichlet case, killed Brownian paths were sampled by running random walks until they are absorbed on the boundary and $u(x)$ is evaluated as an average of the boundary values at the first hitting positions on the boundary. On the other hand, for the Neumann condition, while $u(x)$ is also given as a weighted average of the Neumann data at hitting positions of RBM on the boundary, the weight is related to the boundary local time of RBM. This is a noteworthy point when we compare the probabilistic solutions of the two boundary value problems and try to understand the formula in (3.2.2).

To see the existence of the infinite integral in (3.2.2), we introduce a Gauge function

$$G_q(x) = E^{x_0}\left[\int_0^\infty e_q(t)L(ds)\right], \tag{3.2.3}$$

which is always a positive function of q.

Theorem 6. Let D be a bounded domain in R^d. If the gauge G_q is finite at one point in $\bar{D}$ then it is bounded on $\bar{D}$.

Theorem 7. For any $\phi_2(x) \in L^\infty(\partial D)$, if the gauge function G_q is finite on $\bar{D}$, then there is a unique weak solution to the Neumann boundary problem (3.2.1).

Theorem 6 and Theorem 7 together ensure the existence and thus validity of the integral defined under the condition that G_q is finite.

The "weak solution" mentioned in Theorem 7 is understood under the martingale formulation which initially brought up by [Hsu, ref 19]. Though the formulation is completely different from the weak solution in classical theory, they are essentially equivalent if assuming $u \in C^2(D) \cap C^1(\bar{D})$.

Definition 3. A bounded measurable function u on $\bar{D}$ is called a weak solution of the Neuamnn problem (3.2.1) if for all $x \in \bar{D}$,

$$M_\phi^u(t) = u(X_t) - u(X_0) + \frac{1}{2}\int_0^t \phi(X_s)L(ds) + \int_0^t qu(X_t)ds \tag{3.2.4}$$

is a continuous P^x-martingale.

Theorem 8. Let u be continuous function on $\bar{D}$. The following two conditions are equivalent:

(a) M_ϕ^u defined in (3.2.4) is a continuous P^x-martingale for all $x \in \bar{D}$.

(b) For any $f \in C_\partial^2(D)$, we have

$$\int_D u(x)\left(\frac{\Delta}{2} + q\right) f(x)m(dx) = -\frac{1}{2}\int_{\partial D} \phi_2(x)f(x)\sigma(dx), \tag{3.2.5}$$

The above theorem demonstrates the equivalence of the martingale formulation and the integral formulation of the weak solution of Neumann problem when u is continuous. If the domain D has a C^3 boundary, q is a Feynman-Kac functional and G_q is finite, and ϕ_2 is bounded on ∂D, the solution defined in (3.2.2) is bounded and continuous. Thus, according to Theorem 8 the form (3.2.2) suggests it is a weak solution in the classical sense. Besides, it should be noted that the martingale formulation does not introduce the test functions.

3.3 Robin Problem

3.3.1 Third boundary value problem

For the same time-independent Schrödinger equation with Robin boundary conditions,

$$\begin{cases} \dfrac{1}{2}\Delta u + q(x)u = 0, \quad x \in D; \\ \dfrac{\partial u}{\partial n} - c(x)u = \phi_3(x), \quad x \in \partial D. \end{cases} \tag{3.3.1}$$

A generalization of Feynman-Kac formula gives the probabilistic solution as follows,

$$u(x) = E^{x_0}\left\{\int_0^{\infty} e_q(t)\hat{e}_c(t)\phi_3(X_t)dL_t\right\}. \tag{3.3.2}$$

Again, X_t is a SRBM initiating at x_0. The term Feynman-Kac functional $e_q(t)$, also appeared in the Neumann problem (3.2.1), is defined as

$$e_q(t) = \exp\left[\int_0^t q(X_s)\,ds\right], \tag{3.3.3}$$

and a second functional is introduced for the Robin boundary problem,

$$\hat{e}_c(t) = exp\left[\int_0^t c(X_s)dL_s\right]. \tag{3.3.4}$$

Now (3.3.2) may be written as

$$u(x) = E^{x}\left\{\int_0^{\infty} exp\left[\int_0^t (q(X_s)ds + c(X_s)dL_s)\right]\phi_3(X_t)dL_t\right\}. \tag{3.3.5}$$

The existence of the integral defined under the new measure L_t in (3.3.5) will be shown by a similar construction of gauge function as in the Neumann case.

Definition 4. Define the Gauge for system (2.3.2) to be

$$G(x) = E^{x_0}\left[\int_0^{\infty} \hat{e}_c(t)e_q(t)dL_t\right]. \tag{3.3.6}$$

Theorem 9. Let D be a bounded domain in R^d. If there exists an $x_c \in \bar{D}$ such that $G(x_c)$ is finite, then the function G is continuous and bounded on $\bar{D}$.

Theorem 10. For any $\phi_3(x) \in L^{\infty}(\partial D)$, if the gauge function G is finite on $\bar{D}$, then there is a unique weak solution to the Robin boundary problem (3.3.1).

Moreover, the weak solution under martinagle formulation will be

Definition 5. A function u is called a weak solution of the third problem (3.3.1) if, for all $x \in \bar{D}$,

$$M^u_{\phi_3}(t) = u(X-t) - u(X_0) + \int_0^t c(X_s)u(X_s)dL_s + \int_0^t \phi_3(X_s)dL_s + \int_0^t q(X_s)u(X_s)ds \quad (3.3.7)$$

is a continuous P^x-martingale.

Next theorem shows the equivalence of weak solutions under the martingale formulation and classical sense.

Theorem 11. The function u is a weak solution of (4.1.3) in the sense of Definition 5 if and only if it is a continuous weak solution in the classical sense.

3.3.2 The connection with the Neumann problem

Recall the definition of the local time in Chapter 2 (2.3.1), we have the following approximation

$$L(t) \approx \frac{1}{\varepsilon}\int_0^t I_{D_\varepsilon}(X_s)ds, \quad (3.3.8)$$

thus,

$$dL(s) \approx \frac{1}{\varepsilon} I_{D_\varepsilon}(X_s)ds. \quad (3.3.9)$$

Therefore, (3.3.5) can be modified as

$$u(x) \approx E^x\left\{\int_0^\infty exp\left[\int_0^t \left(q(X_s) + \frac{1}{\varepsilon}c(X_s)I_{D_\varepsilon}(X_s)\right)ds\right]\phi_3(X_t)dL_t\right\}, \quad (3.3.10)$$

It can also be shown that as ε goes to zero, (3.3.10) converges to (3.3.9) uniformly on $\bar{D}$.

As (3.3.10) resembles the Feyman-Kac formula for the Neumann problem with a modified $q(x)$ [14], it indicates a connection between the Robin and the Neumann problems,

namely, we may introduce

$$q_\varepsilon(x) = q(x) + \frac{1}{\varepsilon} c(x) I_{D_\varepsilon}(x), \tag{3.3.11}$$

then, the Robin boundary problem (3.3.1) can be viewed as a limiting case ($\varepsilon \to 0$) of Neumann problems

$$\begin{cases} \frac{1}{2}\Delta u + q_\varepsilon u = 0, \quad in\ D; \\ \qquad \frac{\partial u}{\partial n} = \phi, \quad on\ \partial D. \end{cases} \tag{3.3.12}$$

3.4 Mixed Boundary Problem

To our concern, we only consider mixed Neumann and Robin boundary conditions in a bounded domain D with $\partial D = B_1 \cup B_2$.

$$\begin{cases} \frac{1}{2}\Delta u + q(x)u = 0,\ x \in D \\ \frac{\partial u}{\partial n}(x) = \phi_2(x),\ x \in B_1 \\ \frac{\partial u}{\partial n}(x) - cu(x) = \phi_3(x),\ x \in B_2 \end{cases} \tag{3.4.1}$$

From the previous two sections, we have the probabilistic solution to $(3.4.1)$ is

$$u(x) = E^x \left\{ \int_0^\infty \hat{e}_c(t) e_q(t) \phi_3(X_t) dL(t) \right\} + \frac{1}{2} E^x \left\{ \int_0^\infty e_q(t) \phi_2(X_t) dL(t) \right\}. \tag{3.4.2}$$

where X_t is the standard reflecting Brownian motion and $L(t)$ is the corresponding local time.

The two integrals correspond to the two different boundary conditions. The first expectation only calculates the average information obtained on the Robin boundary while the second expectation cumulates the Neumann values w.r.t. local time along the Neumann boundary.

The application of the mixed boundary value problem will be discussed in Chapter 6.

CHAPTER 4: WALK ON SPHERES METHOD

Random walk on spheres (WOS) method was first proposed by Müller [23], which can solve the Dirichlet problem for the Laplace operator efficiently. Actually, the general linear elliptic operator

$$l(u) = \sum_{i,j=1}^{N} a_{ij}(x)\frac{\partial^2 u}{\partial x_i \partial x_j} + \sum_{i=1}^{N} b_j(x)\frac{\partial u}{\partial x_i} \tag{4.0.1}$$

is allowed for the Dirichlet problem. Here $a_{ij}(x), b_j(x)$ are C^2 functions in the domain. We will first briefly review Dirichlet Problem and this method and then show how it can be adapted for RBM and the Neumann problem in latter chapters.

4.1 Review of Dirichlet Problem

For the Poisson equation with a Dirichlet boundary condition,

$$\begin{aligned} L(u) &= \sum_{i,j=1}^{n} a_{ij}(x)\frac{\partial^2 u}{\partial x_i \partial x_j} = f(x), x \in D, \\ u|_{\partial D} &= \phi(x), x \in \partial D. \end{aligned} \tag{4.1.1}$$

where $a_{ij} = \delta_{ij}$.

The probabilistic representation of the solution is [11][12]

$$u(x) = E^x(\phi(X_{\tau_D})) + E^x\left[\int_0^{\tau_D} f(X_t)dt\right], \tag{4.1.2}$$

where X_t is the standard Brownian motion

$$dX_t = dB_t. \tag{4.1.3}$$

The expectation in (4.1.2) is taken over all sample paths starting from x and τ_D is the first exit time for the domain D. This representation holds true for general linear elliptic PDEs. For the Neumann boundary condition, similar formulas can be obtained [14][4]. However different measures on the boundary ∂D will be used in the mathematical expectation.

In order to illustrate the WOS method for the Dirichlet problem, let us consider the Laplace equation where $f = 0$ in (4.1.1).

The solution to the Laplace equation can be rewritten in terms of a measure μ_D^x defined on the boundary ∂D,

$$u(x) = E^x(\phi(X_{\tau_D})) = \int_{\partial D} \phi(y) d\mu_D^x, \tag{4.1.4}$$

where μ_D^x is the so-called harmonic measure defined by

$$\mu_D^x(F) = P^x\left\{X_{\tau_D} \in F\right\}, F \subset \partial D, x \in D. \tag{4.1.5}$$

It can be shown that the harmonic measure is related to the Green's function for the domain with a homogeneous boundary condition,

$$\begin{cases} -\Delta g(x,y) = \delta(x-y), & x \in D, \\ \\ g(x,y) = 0, & x \in \partial D \end{cases}. \tag{4.1.6}$$

By the third Green's identity,

$$u(x) = \int_{\partial D} \left[u(y) \frac{\partial g(y,x)}{\partial n} - g(y,x) \frac{\partial u}{\partial n}(y) \right] dS_y, \tag{4.1.7}$$

and using the zero boundary condition of g, we have

$$u(x) = \int_{\partial D} u(y) \frac{\partial g(y,x)}{\partial n} dS_y, \tag{4.1.8}$$

where dS_y denotes the surface measure at point y on the boundary. Comparing (4.1.4) with (4.1.8), we can see that the hitting probability $\mu_D^x([y, y+dS_y]) = p(x,y)dS_y$ is given by

$$p(x,y) = -\frac{\partial g(x,y)}{\partial n_y}. \tag{4.1.9}$$

For instance, the Green's function for a ball for this purpose is given as

$$g(x,y) = -\frac{1}{4\pi|x-y|} + \frac{1}{4\pi|x-y^*|}, \tag{4.1.10}$$

where y^* is the inversion point of y with respect to the sphere [27].

Then through implementation of boundary element method, one may obtain the numerical solution to (4.1.8) at any interior point x.

4.2 Walk on Spheres Method

Definition 6. *The Spherical Process* Given a domain $D \subset R^d$ and fixed point $x \in D \cup \partial D$, then the d-dimensional Spherical process originating from x is $\Phi(x)$, where

(a) $\Phi(x) = \{S(x,\phi), 0 \leq \phi \leq 1\}$;

(b) Each ϕ determines the points in the set $S(x,\phi) = \{P_{i+1}(x,\phi), i = 0,1,...\}$ generated as follows:

   i. The point $P_0(x,\phi) = x$, specifies the d-dimensional sphere $K(P_0)$ contained in D.

   ii. The point $P_1(x,\phi)$ is selected uniformly on $K(P_0)$.

   iii. The point $P_{i+1}(x,\phi)$ is determined recursively from $P_i(x,\phi)$ and $K(P_i)$ in the same mannar as $P_1(x,\phi)$ was determined from $P_0(x,\phi)$.

(a) WOS within the domain

(b) WOS (with a maximal step size for each jump) within the domain

Figure 1: Walk on Spheres method

Theorem 12. Given any point x belong to a domain D with boundary ∂D, then with probability 1, the spherical process originating from x converges to a point on ∂D.

Given an interior point x, the Brownian motion process can be simulated by spherical processes as long as the domain is homogeneous. The first ball is drawn at the center of x, then the probability of the BM exiting a portion of the boundary of the ball will be proportional to the portion's area. According to Theorem 12, all sample functions of Brownian motion processes starting in the domain intersects the boundary ∂D almost surely. Therefore, sampling a Brownian path by drawing balls within the domain, regardless of how the path navigates in the interior before hitting the boundary, can significantly reduce the path sampling time. To be more specific, given a starting point x inside the domain D, we simply draw a ball of the largest possible radius fully contained in D and then the next location of the Brownian path on the surface of the ball can be sampled, using a uniform distribution on the sphere, say at x_1. Treat x_1 as the new starting point, draw a second ball fully contained in D, make a jump from x_1 to x_2 on the surface of the second ball as before. Repeat this procedure until the path hits an absorption ε-shell of the domain [13]. When this happens, we assume that the path has hit the boundary ∂D (see Fig. 1 for an illustration).

Next we define an estimator of (4.1.4) by

$$u(x) \approx \frac{1}{N} \sum_{i=1}^{N} \phi(x_i), \tag{4.2.1}$$

where N is the number of Brownian paths sampled and x_i is the first hitting point of each path on the boundary. Using a jump size (radius of the ball) δ on each step for the WOS, we expect to take $O(1/\delta^2)$ steps for a Brownian path to reach the boundary [2]. To speed up, maximum possible size for each step would allow faster first hitting on the boundary. In the next chapter, the WOS approach will be employed to simulate RBM paths as illustrated in Fig. 1(b).

CHAPTER 5: NUMERICAL METHODS AND RESULTS

Simulations of diffusion paths can be done by random walks methods [20][2] [23][24] either on a lattice or in continuum space. In some cases such as for the Poisson equation, the Feynman-Kac formula has a pathwise integral requiring the detailed trajectory of each path. Moreover, one may need to adopt random walks on a discrete lattice in order to incorporate inhomogeneous source terms. As for the continuum space approach, the Walk on Spheres (WOS) method is preferred where the path of diffusion process within the domain does not appear in the Feynman-Kac formula. For instance, the WOS method was implemented in [27] to solve Laplace equation with Dirichlet boundary condition at some interested points and a local boundary integral equation is used to obtain a DtN mapping.

This chapter focuses on simulation of reflecting Brownian motion paths, calculation of boundary local time and how it can be incorporated into Feynman-Kac formulas under different boundary conditions.

5.1 Simulation of Reflecting Brownian Paths

A standard reflecting Brownian motion path can be constructed by reflecting a standard Brownian motion path back into the domain whenever it crosses the boundary. So in principle, the simulation of RBM is reduced to that of BM.

It is known that standard Brownian motion can also be constructed as the scaling limit of a random walk on a lattice so we can model BM by a random walk with proper scaling (see

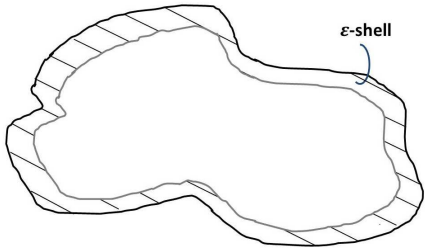

Figure 2: A ε-region for a bounded domain in R^3

Appendix for details). However, it turns out that the WOS method is the preferred method to simulate BM for our purpose [24] (see Remark 5 for details). As mentioned before, an ε-shell is chosen around the boundary as the termination region in the Dirichlet case. Here we follow a similar strategy by setting up a ε-region but allowing the process X_t to continue moving after it reaches the ε-region instead of being absorbed.

Fig.2 shows a strip region with width ε near the boundary for a bounded domain. In a spherical domain, the ε-region is simply an ε-shell near the boundary of width ε. Denote $M_\varepsilon(D)$ as the ε-region and $I_\varepsilon(D)$ as the remaining interior region $D\backslash M_\varepsilon(D)$.

Recall the discussion of the WOS in the previous section. For a BM starting at a point x in the domain, we draw a ball centered at x. The Brownian path will hit the spherical surface with a uniform probability as long as the ball does not overlap the domain boundary ∂D. The balls are constructed so that the jumps are as large as possible by taking the radius of the ball to be the distance to the boundary ∂D. We repeat this procedure until the path reaches the region $M_\varepsilon(D)$. Here, we continue the WOS in $M_\varepsilon(D)$ but with a fixed radius Δx much smaller than ε. In order to simulate the path of RBM, at some points of the time the BM path will run out of the domain. For this to happen, the radius of WOS is increased to $2\Delta x$ when the path is close to boundary at a distance less than Δx. In this way, the BM path will have a chance to get out of the domain, and when that happens, we then pull it back to

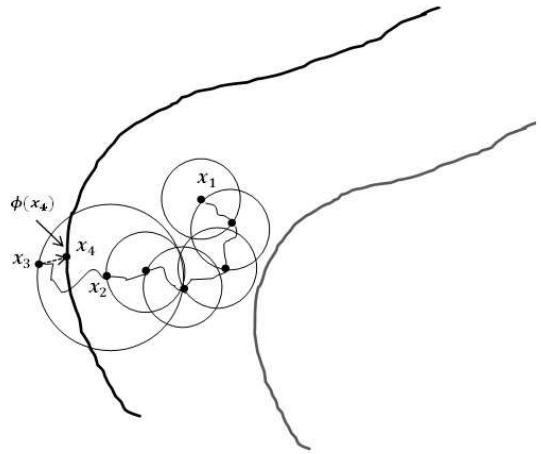

Figure 3: WOS in the ε-region. BM path hits x_1 in ε-region for the first time. Then the radius of sphere is changed to Δx, the path continues until it arrives at x_2 whose distance to ∂D is smaller or equal to Δx. Then the radius of the ball is enlarged to $2\Delta x$ so that the path has a chance to run out of the domain at x_3. If that happens, we pull back x_3 to x_4 which is the closest point to x_3 on the boundary. Record $\phi(x_4)$, and continue WOS-sampling the path starting at x_4.

the nearest point on the boundary along the normal of the boundary. Afterwards, the BM path will continue as before.

In summary, a reflecting Brownian motion path is simulated by the WOS method inside D. Once it enters the ε-region $M_\varepsilon(D)$, the radius of WOS changes to a fixed value, either Δx or $2\Delta x$, depending on its current distance of the Brownian particle to the boundary. Once the path reaches a point on the boundary after the reflection, the radius of WOS changes back to Δx. Fig.3 illustrates the movement of RBM in the ε-region $M_\varepsilon(D)$. As time progresses, we expect the path hits the boundary at some time instances and lies in either $I_\varepsilon(D)$ or $M_\varepsilon(D)$ at others. A sample path of RBM is shown in Fig.4 within a cube of size 2.

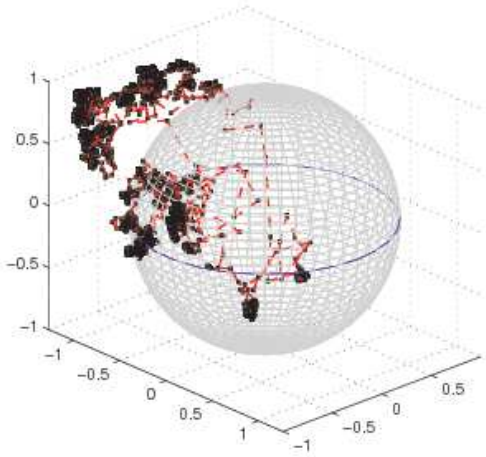

Figure 4: A RBM path within a cube in R^3

5.2 Computing the Boundary Local Time

5.2.1 Average exit time for one step of WOS

For the random walk on a lattice as in Fig. 5 to converge to a continuous BM, a relationship between Δt and Δx in R^3 will be needed and is shown to be

$$\Delta t = \frac{(\Delta x)^2}{3}. \tag{5.2.1}$$

The following is a proof of this result (See [5] for a reference). The density function of standard BM satisfies the following PDE [14]

$$\frac{\partial p}{\partial t} = \frac{1}{2}\Delta_x p(t,x,y)\ . \tag{5.2.2}$$

By using a central difference scheme and changing p to v, equation (5.2.2) becomes

$$\frac{v^{n+1}_{i,j,k} - v^n_{i,j,k}}{\Delta t} = \frac{1}{2}\frac{v^n_{i+1,j,k} + v^n_{i-1,j,k} + v^n_{i,j+1,k} + v^n_{i,j-1,k} + v^n_{i,j,k+1} + v^n_{i,j,k-1} - 6v^n_{i,j,k}}{(\Delta x)^2}\ , \tag{5.2.3}$$

where i, j, k are the indices of grid points on the lattice with respect to the three axes.

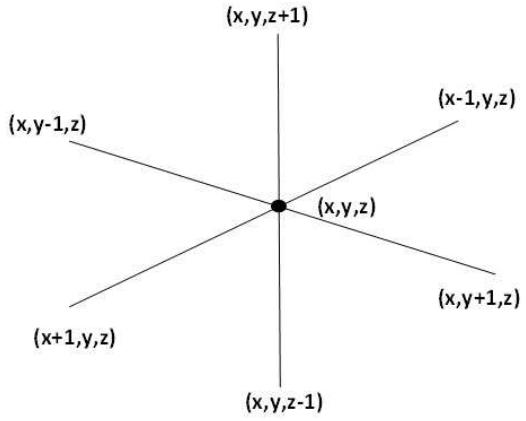

Figure 5: Central difference scheme in R^3

Reorganizing (5.2.3) and letting $\lambda = \Delta t/(2(\Delta x)^2)$, we have

$$v_{i,j,k}^{n+1} = \lambda v_{i+1,j,k}^{n} + \lambda v_{i-1,j,k}^{n} + \lambda v_{i,j+1,k}^{n} + \lambda v_{i,j-1,k}^{n} + \lambda v_{i,j,k+1}^{n} + \lambda v_{i,j,k-1}^{n} + (1-6\lambda) v_{i,j,k}^{n} \,, \tag{5.2.4}$$

By setting $\lambda = \frac{1}{6}$, we have

$$v_{i,j,k}^{n+1} = \frac{1}{6} v_{i+1,j,k}^{n} + \frac{1}{6} v_{i-1,j,k}^{n} + \frac{1}{6} v_{i,j+1,k}^{n} + \frac{1}{6} v_{i,j-1,k}^{n} + \frac{1}{6} v_{i,j,k+1}^{n} + \frac{1}{6} v_{i,j,k-1}^{n}. \tag{5.2.5}$$

Using the initial condition ϕ, we have

$$v_{i,j,k}^{n+1} = \sum_{i',j',k'} C_{i',j',k'} \phi \left(\sum_{l=1}^{n} \vec{\eta}_l \right), \tag{5.2.6}$$

where

$$\vec{\eta}_l = \begin{cases} (-h,0,0)^T, & \text{prob} = \dfrac{1}{6} \\ (h,0,0)^T, & \text{prob} = \dfrac{1}{6} \\ (0,h,0)^T, & \text{prob} = \dfrac{1}{6} \\ (0,-h,0)^T, & \text{prob} = \dfrac{1}{6} \\ (0,0,h)^T, & \text{prob} = \dfrac{1}{6} \\ (0,0,-h)^T, & \text{prob} = \dfrac{1}{6} \end{cases}, \tag{5.2.7}$$

and

$$\sum_{l=1}^{n} \vec{\eta}_l = \begin{pmatrix} -n+2i'+i \\ -n+2j'+j \\ -n+2k'+k \end{pmatrix} h. \tag{5.2.8}$$

Let $\vec{\eta}_l = (x_l, y_l, z_l)^T$, then

$$x_l = \begin{cases} -h, \text{ prob} = \dfrac{1}{6} \\ h, \text{ prob} = \dfrac{1}{6} \\ 0, \text{ prob} = \dfrac{2}{3} \end{cases}, \tag{5.2.9}$$

for each l. We known that y_l, z_l have the same distribution as x_l.

Notice that the covariance between any two of x_l, y_l, z_l is zero, i.e. $E(x_l y_l) = 0, E(y_l z_l) = 0$ and $E(x_l z_l) = 0$. So $E(\sum_{i=1}^n x_l \sum_{i=1}^n y_l) = 0, E(\sum_{i=1}^n y_l \sum_{i=1}^n z_l) = 0$ and $E(\sum_{i=1}^n x_l \sum_{i=1}^n z_l) = 0$. According to the central limit theorem, we have

$$\sum_{i=1}^{n} x_l \overset{D}{=} N\left(0, \frac{nh^2}{3}\right) \ as \ \ n \to \infty. \tag{5.2.10}$$

The same assertion holds for $\sum_{i=1}^n y_l$ and $\sum_{i=1}^n z_l$.

Since $\lambda = \frac{\Delta t}{2(\Delta x)^2} = \frac{1}{6}$, then $h^2 = 3k$ and hence $\frac{nh^2}{3} = nk = t$. Therefore $\sum_{i=1}^n x_l \ \sim N(0,t)$

as $n \to \infty$. So are $\sum_{i=1}^{n} y_l$ and $\sum_{i=1}^{n} z_l$.

Recall that the covariance between any pair of $\sum_{i=1}^{n} x_l$, $\sum_{i=1}^{n} y_l$, and $\sum_{i=1}^{n} z_l$ is zero, that $\sum_{i=1}^{n} x_l$,$\sum_{i=1}^{n} y_l$ and $\sum_{i=1}^{n} z_l$ become independent normal random variables as $n \to \infty$. Hence,

$$C_{i',j',k',n} = P\left\{ \sum_{l=1}^{n} \vec{\eta}_l = \begin{pmatrix} -n+2i'+i \\ -n+2j'+j \\ -n+2k'+k \end{pmatrix} h = \begin{pmatrix} \sum_{i=1}^{n} x_l \\ \sum_{i=1}^{n} y_l \\ \sum_{i=1}^{n} z_l \end{pmatrix} \right\} \xrightarrow{D} \frac{1}{(2\pi t)^{3/2}} e^{\frac{-\|\vec{x}-\vec{x_0}\|^2}{2t}}, \quad (5.2.11)$$

and

$$v_{i,j,k}^{n+1} = \sum_{i',j',k'} C_{i',j',k',n} \phi(\sum_{l=1}^{n} \vec{\eta}_l) \to \iiint_{R^3} \frac{1}{(2\pi t)^{3/2}} e^{\frac{-\|\vec{x}-\vec{x_0}\|^2}{2t}} \phi(\vec{x}) d\vec{x}, \quad (5.2.12)$$

which coincides with the density function of the 3-d standard BM.

In conclusion, when $\frac{\Delta t}{2(\Delta x)^2} = \frac{1}{6}$, i.e. $\Delta t = \frac{(\Delta x)^2}{3}$ or $\sqrt{dt} = \frac{dx}{\sqrt{3}}$, the central difference scheme converges to the standard BM in 3-d. Generally, the result can be extended to d-dimensional Euclidean space and the result will be $\Delta t = \frac{(\Delta x)^2}{d}$.

5.2.2 Computing the Boundary Local Time

Two equivalent forms of the local time have been given in (2.3.1) and (2.3.3). Here we will show how the ε-region for the construction of the RBM in Fig.3 can also be used for the calculation of the local time. When the ε-region is thin enough, i.e. $\varepsilon \ll 1$, an approximation of (2.3.1) is given in (3.3.8), which is the occupation time that RBM X_s sojourns within the ε-region during the time interval $[0,t]$. A close look at (3.3.8) reveals that only the time spent near the boundary is involved and the specific moment when the path enters the ε-region has no effect on the calculation of $L(t)$.

Suppose $x \in D$ is the starting point of a Brownian path, which is simulated by the WOS method. Once the path enters the ε-region, the radius of WOS is changed to Δx or $2\Delta x$. It is known that the elapsed time Δt for a step of a random walk on average is proportional to the square of the step size, in fact, $\Delta t = (\Delta x)^2/d, d = 3$ when Δx is small (see the previous section), which also applies to WOS moves (See Remark 5 for details). Therefore, we can obtain an approximation of the local time $L(dt)$ by counting the number of steps the path spent inside $M_\varepsilon(D)$ multiplied by the time elapsed for each step, i.e.

$$L(dt) = L(t_j - t_{j-1}) \approx \frac{\int_{t_{j-1}}^{t_j} I_{D_\varepsilon}(X_s)ds}{\varepsilon} = (n_{t_j} - n_{t_{j-1}})\frac{(\Delta x)^2}{3\varepsilon}, \tag{5.2.13}$$

where dt is defined as time increment $t_j - t_{j-1}$ and $n_{t_j} - n_{t_{j-1}}$ is the number of steps that WOS steps remain in the ε-region during the time interval $[t_{j-1}, t_j]$. Note that in our method within the $\varepsilon-$region, the radius of the BM may be Δx or $2\Delta x$, which means the corresponding elapsed time of one step for local time will be either $(\Delta x)^2/3$ or $(2\Delta x)^2/3$. If we absorb the factor 4 into n_t, we will still have $(5.2.13)$. Fig.6 gives a sample path of the simulated local time associated with the RBM in Fig.4.

In practical implementation, we treat n_t as a vector of entries of increasing value, the increment of each component of n_t over the previous one after each step of WOS will be 0, 1 or 4, corresponding to the scenarios that X_t is out of the ε-region, in the ε-region while sampled on the sphere of a radius Δx, or in the ε-region while sampled on the sphere of a radius $2\Delta x$, respectively.

Remark 4. (Alternative way to compute local time $L(t)$) From $(2.3.3)$, the local time increases if and only if the RBM path hits the boundary, which implies that the time before the path hits the boundary makes no contribution to the increment of the local time. Thus,

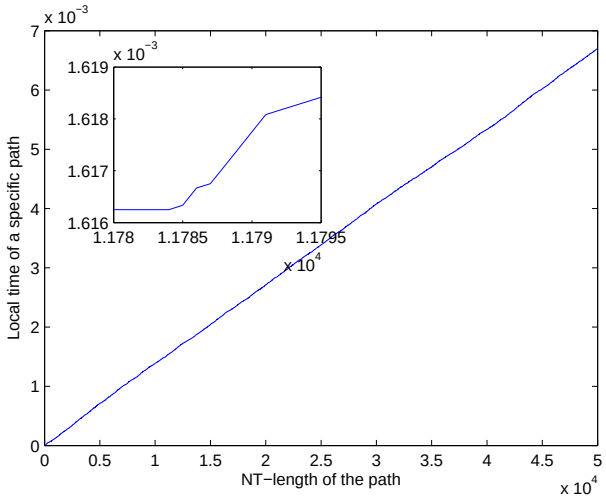

Figure 6: Boundary local time (4.1.10) increases when the path runs into the region $M_\varepsilon(D)$. The insert shows the piecewise linear profile of the local time path with flat level regions. By our construction, most of the path will fall into the ε-region. If x-axis changes to time line, the graph should be more flatter than it appears here which implies that boundary local time increases only on a small set.

a WOS method with a changing radius can also be used with (2.3.3). Specifically, we divide the time interval $[0,t]$ into to N small subintervals of equal length. In each $[t_i,t_{i+1}]$ the Brownian path will move $2\Delta x$ or Δx with the WOS method when the current path lies within a distance less or more than Δx to the boundary. If the path hits or crosses the boundary within $[t_i,t_{i+1}]$, then $L(t)$ will increase by $\sqrt{\pi/2}\sqrt{t_{i+1}-t_i}$.

Remark 5. (Approximating RBM by WOS or random walks on a lattice - a comparison) There are two ways to find approximation to Brownian paths inside the region $M_\varepsilon(D)$ and construct their reflections once they get out of the domain. One way is by using the WOS approach as described in the begining of the chapter . The other is in fact to use a random walk on a lattice inside $M_\varepsilon(D)$. Both belong to the random walk techniques while WOS prevails in homogeneous media without consideration of the whole trajectories of paths and random walk on a lattice is widely used in various other situations. In the second approach,

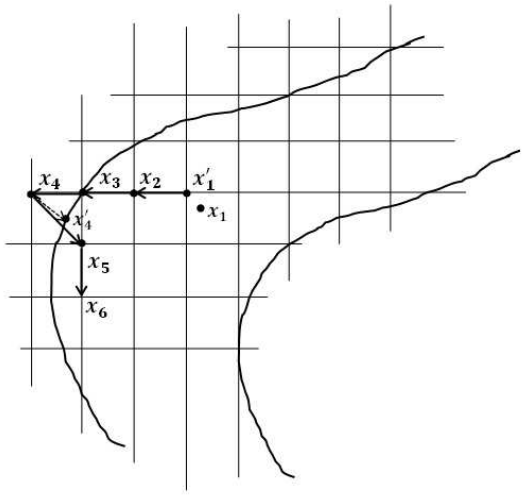

Figure 7: Random walks on the ε-region. A BM path hits $x_1 \in M_\varepsilon(D)$ by the WOS method. Replace x_1 by the nearest grid point x_1'. Then several steps of random walks will make a path as $x_2 \to x_3 \to x_4$. Since $x_4 \notin D$, we push it back along the normal line (dash arrow) to x_4' then replace it by the closest grid point within domain (solid arrow) x_5. Here path crosses the boundary at $x_4' \in \partial D$. Then continue the random walk as usual at x_6.

as illustrated in Fig.7, a grid mesh is set up over $M_\varepsilon(D)$ and the random walk takes a one-step walk on the lattice until the path goes out of the domain and then it will be pushed back to the nearest lattice point inside $M_\varepsilon(D)$. And the elapsed time for a Δx walk is on average $(\Delta x)^2/3$ as shown in Appendix. The boundary local time $L(t)$ can still be calculated as in $(2.3.3)$. The problem with this approach is that a Brownian motion actually should have equal probability to go in all directions in the space while a random walk on the lattice only considers six directions in R^3. This limitation was found in our numerical tests to lead to insufficient accuracy in simulating reflecting Brownian motions for our purpose.

Meanwhile, the WOS method in the ε-region $M_\varepsilon(D)$ has a fixed radius Δx, which enables us to calculate the boundary local time by $(5.2.13)$ since the elapsed time of a Δx move in R^3 on average still remains to be $(\Delta x)^2/3$. This conclusion can be heuristically justified by considering points on the sphere as linear combinations of the directions along the three

axes, which implies that the average time that the path hits the sphere with radius Δx should also be the same. As discussed before, if the path comes within a distance very close to the boundary, say less than Δx, the radius of the WOS method is increased to $2\Delta x$ so that it will have a chance to run out of the domain and then be pushed back to the nearest point on the boundary to effect a hit of the RBM on the boundary.

5.3 Probabilistic Representation for Various Boundary Conditions

5.3.1 Neumann Boundary Problem

Finally, with the boundary local time of RBM available, we can come to the approximation of the Neumann problem solution $u(x)$ using the probabilistic approach (3.3.4). First of all, we will need to truncate the infinite time duration required for the RBM path X_t in (3.2.2) to a finite extent for computer simulations. The exact length of truncation will have to be numerically determined by increasing the length until a convergence is confirmed (namely, the approximation to $u(x)$ does not improve within a prescribed error tolerance between two different choices of truncation times under same number of sampled paths). Assume that the time period is limited to from 0 to T, then by a Monte Carlo sampling of RBM paths, an approximation of (3.2.2) will be

$$\widetilde{u}(x) = \frac{1}{2\varepsilon} \sum_{i=1}^{N} \left[\int_0^T \phi(X_t^i) I_{\partial D}(X_t^i) \int_t^{t+dt} I_{D_\varepsilon}(X_s^i) ds \right], \tag{5.3.1}$$

where $X_t^i, i = 1, ..., N$ are stochastic processes sampled according to the law of RBM.

Next, let us see how the RBM can be incorporated into the representation formula once its path is obtained.

Associate the time interval $[0, T]$ with the number of steps NT of a sampling path, NT

will give the total length of each path. Then, the integral inside the square bracket in (5.3.1) can be transformed into j

$$\sum_{j'=1}^{NT}\left(\phi(X_{t_j}^i)I_{\partial D}(X_{t_j}^i)\int_{t_{j-1}}^{t_j} I_{D_\varepsilon}(X_s^i)ds\right), \tag{5.3.2}$$

where j' stands for the $j'-$th step of the WOS method, and j corresponds to a step for which $X_{t_j}^i \in \partial D$ and summation is only done over those j's.

As the integral in (5.3.2) is in fact the occupation time as shown in (5.2.13), (5.3.2) becomes

$$\sum_{j'=1}^{NT}\left(\phi(X_{t_j}^i)I_{\partial D}(X_{t_j}^i)(n_{t_j}-n_{t_{j-1}})\frac{(\Delta x)^2}{3}\right). \tag{5.3.3}$$

As a result, an approximation to the PDE solution $\widetilde{u}(x)$ becomes

$$\widetilde{u}(x)=\frac{1}{2\varepsilon}\sum_{i=1}^{N}\left[\sum_{j'=1}^{NT}\left(\phi(X_{t_j}^i)I_{\partial D}(X_{t_j}^i)(n_{t_j}-n_{t_{j-1}})\frac{(\Delta x)^2}{3}\right)\right]. \tag{5.3.4}$$

Theoretically speaking, ε should be chosen much larger than Δx. Here, we take $\varepsilon = k\Delta x$, $k>1$ is an integer, which will increase as Δx vanishes to zero. Then, (5.3.4) reduces to

$$\begin{aligned}\widetilde{u}(x)&=\frac{1}{2k\Delta x}\sum_{i=1}^{N}\left[\sum_{j=1}^{NT}\left(\phi(X_{t_j}^i)I_{\partial D}(X_{t_j}^i)(n_{t_j}-n_{t_{j-1}})\frac{(\Delta x)^2}{3}\right)\right]\\&=\frac{\Delta x}{6k}\sum_{i=1}^{N}\left[\sum_{j=1}^{NT}\left(\phi(X_{t_j}^i)I_{\partial D}(X_{t_j}^i)(n_{t_j}-n_{t_{j-1}})\right)\right],\end{aligned} \tag{5.3.5}$$

which is the final numerical algorithm for the Neumann problem. In the following we present the general implementation of this numerical algorithm.

Let x be any interior point in D where the solution $u(x)$ for the Neumann problem is sought. First, we define the ε-region $M_\varepsilon(D)$ near the boundary. For each one of N RBM paths, the following procedure will be executed until the length of the path reaches a prescribed length given by $NT\cdot\Delta x$:

1. If $x \notin M_\varepsilon(D)$, predict next point of the path by the WOS with a maximum possible radius until the path locates near the boundary within a certain given distance ε, say $\varepsilon = 3\Delta x$ (hit the ε-region $M_\varepsilon(D)$). If $x \in M_\varepsilon(D)$, $l(t_i) = 1(4)$; otherwise, $l(t_i) = 0$. Here $l(t)$ is the unit increment of $L(t)$ at time t.

2. If $x \in M_\varepsilon(D)$, use the WOS method with a fixed radius Δx to predict the next location for Brownian path. Then, execute one of the two options:

   Option 1. If the path happens to hit the domain boundary ∂D at x_{t_i}, record $\phi(x_{t_i})$.

   Option 2. If the path passes crosses the domain boundary ∂D, then pull the path back along the normal to the nearest point on the boundary. Record the Neumann value at the boundary location.

Due to the independence of the paths simulated with the Monte Carlo method, we can run a large number of paths simultaneously on a computer with many cores in a perfectly parallel manner, and then collect all the data at the end of the simulation to compute the average. **Algorithm 1** gives a pseudo-code for the numerical realization of implementing the WOS in both $I(D)$ and $M_\varepsilon(D)$ regions.

As described in this section, it is quite clear that calculation of the distance to the boundary accounts for a large portion of computing time in our algorithm, especially when the Brownian path is out of the ε-shell. For simple domains like a cube and a sphere in R^3, this distance can be found easily and thus consumes little time. In the ellipsoid case, the distance is still computable which involves the calculation of normal directions and thus requires much more time than the former cases. For more general domains, more efficient

numerical methods are desired.

Algorithm 1: The algorithm for the probabilistic solution of the Laplace equation with the Neumann boundary condition

5.3.2 Robin Boundary Problem

In this section, we only consider the case of the Laplace equation where $q = 0$ in (3.3.1). From (3.3.2),

$$u(x) = E^x \left\{ \int_0^\infty e^{\int_0^t c(X_t)dL_t} f(X_t)dL_t \right\}, \tag{5.3.6}$$

where X_t represents the standard reflecting Brownian motion. For the sake of computer simulation, the time period is truncated into $[0,T]$ to produce an approximation for $u(x)$, i.e.,

$$\tilde{u}(x) = E^x \left\{ \int_0^T e^{\int_0^t c(X_t)dL_t} f(X_t)dL_t \right\}. \tag{5.3.7}$$

We have described the realization of SRBM paths and the calculation of the corresponding local time, as implemented in [30]. A SRBM path can be constructed by pulling back a BM path back onto the boundary whenever it runs out of the domain. Specifically, a SRBM path behaves exactly the same way as a BM which is simulated by the WOS method.

Robin boundaries represent a general form of an insulating boundary condition for convection-diffusion equations where $c(x)$ stands for the positive diffusive coefficients. For our numerical test, we will consider two cases: a positive constant c and a positive function $c(x)$.

- Constant $c(x)$

Example 1 $c(X_t) = -1$

Data: Select integers N and NT, a starting point $X_0 \in D$, step size h and ε-region $M_\varepsilon(D)$ near the boundary.
Output An approximation of $u(X_0)$.

Initialization $L[NT], v[NT], u[N]$, $X = X_0$, $i \leftarrow 1$ and $j \leftarrow 1$;

While $i \leq N$ **do**
  Set $S_i = 0$.
  While $j \leq NT$ **do**
    If $X \in I(D)$ **then** /* If the path has not touched the ε-region */
      Set $L[j] \leftarrow 0$; /*Increment of local time at each step. */
      Set $r \leftarrow d(X, \partial D)$; /* Find the distance to the boundary */
      Randomly choose a point X_1 on $B(X, r)$ then set $X \leftarrow X_1$.
    Else /* The path enters the ε-region */
      Set $r \leftarrow$ h (2h); /* If $d(X, \partial D) > h$ or =0 ($0 < d(X, \partial D) \leq h$) */
      $L[j] \leftarrow 1(4)$; /*local time increases */
      Randomly choose a point X_1 on $B(X, r)$ then set $X \leftarrow X_1$.
      If $X \notin \bar{D}$, **then**
        Find X_j to be the nearest point on ∂D to X and pull X back
        onto ∂D at X_j;
        Set $X \leftarrow X_j$;
        Set $v[j] \leftarrow \phi(X_j)$
      End
    End
    $j \leftarrow j + 1$;
  End
  count $\leftarrow 0$;
  For k=1:NT
    count $\leftarrow$ count + $L[k]$;
    If $v[k] \sim= 0$ **then**
    $u[i] \leftarrow u[i] + \phi(X_k)\cdot$count;
    count $\leftarrow 0$;
  End
  $i \leftarrow i + 1$;
End
Return $\widetilde{u}(X_0) = h \sum_{k=1}^{N} u[k]/N/(6k)$

In this case, (5.3.7) is reduced to

$$u(x) = E^x \left\{ \int_0^\infty e^{\int_0^t -dL_t} f(X_t) dL_t \right\}, \tag{5.3.8}$$

which is equivalent to

$$u(x) = E^x \left\{ \int_0^\infty e^{-L_t + L_0} f(X_t) dL_t \right\}, \tag{5.3.9}$$

or

$$u(x) = E^x \left\{ \int_0^\infty e^{-L_t} f(X_t) dL_t \right\}, \tag{5.3.10}$$

for a starting point x belonging to the interior of the solution domain.

We will truncate the time interval to $[0,T]$, an approximation to (5.3.12) will be

$$\tilde{u}(x) = E^x \left\{ \int_0^T e^{L_t} f(X_t) dL_t \right\}. \tag{5.3.11}$$

Using the fact that

$$dL_t \approx (n_t - n_{t-1}) \frac{(\Delta x)^2}{3\varepsilon}, \tag{5.3.12}$$

we can rewrite (5.3.11) as

$$\tilde{u}(x) = E^x \left\{ \int_0^T e^{-n_t \frac{(\Delta x)^2}{3\varepsilon}} f(X_t)(n_t - n_{t-1}) \frac{(\Delta x)^2}{3\varepsilon} \right\}. \tag{5.3.13}$$

Next, identifying the time interval with the length of sample path NP, we have

$$\tilde{u}(x) = E^x \left\{ \sum_{j'=0}^{NP} e^{-n_{t_j} \frac{(\Delta x)^2}{3\varepsilon}} f(X_{t_j})(n_{t_j} - n_{t_{j-1}}) \frac{(\Delta x)^2}{3\varepsilon} \right\}, \tag{5.3.14}$$

where j' denotes each step of the path and j denotes the steps where the path hits the boundary.

At each step along a path we first evaluate

$$e^{-n_{t_j}\frac{(\Delta x)^2}{3\varepsilon}} f(X_{t_j})(n_{t_j} - n_{t_{j-1}})\frac{(\Delta x)^2}{3\varepsilon},$$

if X_{t_j} hits the boundary, we then compute $f(X_{t_j})(n_{t_j} - n_{t_{j-1}})\frac{(\Delta x)^2}{3\varepsilon}$, followed by multiplying it by $e^{-n_{t_j}\frac{(\Delta x)^2}{3\varepsilon}}$, which uses the cumulative time of L_{t_j} from $t = 0$ to t_j. Finally, the expectation is done via the average over N sample paths.

- Variable $c(x)$

Example 2 $c(X_t) = -|x|$, x is the first component of X_t on the boundary. Similar to Example 1, we have

$$u_{3rd}(x) = E^x \left\{ \int_0^\infty e^{\int_0^t c(X_s)dL_s} f(X_t)dL_t \right\}. \tag{5.3.15}$$

It can be seen that $c(X_s)dL_s$ and $f(X_t)dL_t$ have the same form, so we can handle $c(X_s)dL_s$ exactly the same way as $f(X_t)dL_t$. Then, we have

$$\tilde{u_{3rd}}(x) = E^x \left\{ \sum_{j'=0}^{NP} e^{\sum_{k=0}^{j} c(X_{t_k})(n_{t_k} - n_{t_{k-1}})\frac{h^2}{3\varepsilon}} f(X_{t_j})(n_{t_j} - n_{t_{j-1}})\frac{h^2}{3\varepsilon} \right\}, \tag{5.3.16}$$

where j' denote each step for the path and j denotes the steps where the path hits the boundary.

Notice that the term

$$e^{\sum_{k=0}^{j} c(X_{t_k})(n_{t_k} - n_{t_{k-1}})\frac{h^2}{3\varepsilon}} \tag{5.3.17}$$

cumulates all the information of $c(X_t)$ with respect to the local time from the beginning to the current time. If $c(X_t) = -|x|$, then

$$u_{\tilde{3}rd}(x) = E^x \left\{ \sum_{j'=0}^{NP} e^{-\sum_{k=0}^{j} |x_{t_k}| (n_{t_k} - n_{t_{k-1}}) \frac{h^2}{3\varepsilon}} f(X_{t_j})(n_{t_j} - n_{t_{j-1}}) \frac{h^2}{3\varepsilon} \right\}. \tag{5.3.18}$$

5.3.3 Mixed Boundary Problem

Again, only laplace equations are considered which implies $q(x) = 0$ in (3.4.2) then (3.4.2) is reduced to

$$u_{Mix}(x) = E^x \left\{ \int_0^\infty \hat{e_c}(t) \phi_3(X_t) dL(t) \right\} + \frac{1}{2} E^x \left\{ \int_0^\infty \phi_2(X_t) dL(t) \right\}. \tag{5.3.19}$$

where X_t is the standard reflecting Brownian motion and $L(t)$ is the corresponding local time.

The numerical approximation to (5.3.19) will be

$$u_{\tilde{M}ix}(x) = E^x \left\{ \int_0^T e^{\int_0^t c(X_t) dL(t)} \phi_3(X_t) dL(t) \right\} + \frac{1}{2} E^x \left\{ \int_0^T \phi_2(X_t) dL(t) \right\}. \tag{5.3.20}$$

or

$$u_{\tilde{M}ix}(x) = E^x \left\{ \sum_{j=0}^{NP} e^{\int_0^t c(X_{t_j}) dL(t_j)} \phi_3(X_{t_j}) dL(t_j) \right\} + \frac{1}{2} E^x \left\{ \sum_{j=0}^{NP} \phi_2(X_{t_j}) dL(t_j) \right\}. \tag{5.3.21}$$

Equivalently,

$$u_{\tilde{M}ix}(x) = E^x \left\{ \sum_{j:X_{t_j} \in E}^{NP} e^{\int_0^t c(X_{t_j}) dL(t_j)} \phi_3(X_{t_j}) dL(t_j) \right\} + \frac{1}{2} E^x \left\{ \sum_{j:X_{t_j} \in D}^{NP} \phi_2(X_{t_j}) dL(t_j) \right\}. \tag{5.3.22}$$

5.4 Numerical Results

5.4.1 Neumann Boundary Problem

In this section, we give the numerical results for the Neumann problem in cubic, spherical, ellipsoid and non-convex domains.

To monitor the accuracy of the numerical approximation of the solutions, we select a circle inside the domain, where the solution of the PDE $u(x)$ will be found by the proposed numerical methods, defined by

$$\{(x,y,z)^T = (r\cos\theta_1 \sin\theta_2, r\sin\theta_1 \sin\theta_2, r\cos\theta_2)^T\} \tag{5.4.1}$$

with $r = 0.6$, $\theta_1 = 0, 2\pi/30, 4\pi/30, ..., 2\pi$, $\theta_2 = \pi$ with 15 different θ_1 in ascending order. In addition, a line segment will also be selected as the locations to monitor the numerical solution, the endpoints of the segment are $(0.4, 0.4, 0.6)^T$ and $(0.1, 0, 0)^T$, respectively. Fifteen uniformly spaced points on the circle or the line are chosen as the locations for computing the numerical solutions.

The true solution of the Neumann problem (4.0.1) with the corresponding Neumann boundary data is

$$u(x) = \sin 3x \sin 4y \; e^{5z} + 5. \tag{5.4.2}$$

In the figures of numerical results given below, the blue curves are the true solutions and the red-circle ones are the approximations. The numerical solutions are shifted by a constant so they agree with the exact solution at one point as the Neumann problem is only unique up to an arbitrary additive constant. “Err”indicates the relative error of the approximations.

- Convergence rate study

The analysis of the errors of our numerical methods is complex as it involves several inter-connected factors, the time truncation T, the radius of the WOS sphere inside the ε-layer and the layer's thickness, and the number of Brownian paths.

A cubic domain of size 2 is selected to test the choice of the number of paths and the length of the paths (truncation time duration T) in the numerical formula (5.3.5).Taking the cubic domain avoids a source of errors in computing the projection of the paths onto the domain boundary.

First we consider the proper choice of the truncation length NT parameter of the Brownian paths. The step-size $\Delta x = 5 \times 10^{-4}$ is used as the radius of the WOS inside the ε-region $M_\varepsilon(D)$, namely, the step-size of the random walk approximation of the RBM near the boundary. The strip width ε is chosen to be $3\Delta x$. The number of paths is taken as $N = 2 \times 10^5$. Two choices for the path length parameter $NT = 2.7 \times 10^4$ and $NT = 2.9 \times 10^4$ for the circle ($NT = 2.4 \times 10^4$ and $NT = 2.5 \times 10^4$ for the line segment) are compared to gauge the convergence of the numerical formula in terms of the path truncation. Fig.8 and Fig.9 show the solution and the relative errors in both cases, which indicates that $NT = 2.9 \times 10^4$ and $NT = 2.5 \times 10^4$ will be sufficient to give an error below 3% for the circle and the line segment, respectively, as shown in Fig.9.

It should be noted that the parameter NT for the length of the path (in terms of number of WOS steps) does not correspond to the physical time T. This is due to the fact that no elapsed time estimate is known for a WOS step of a large sphere radius inside the interior of the domain. In theory, the larger the truncation time T, the more accurate is the probabilistic

solution for the Neumann solution. Theoretical variance estimate on the truncation of the time T has been given in [20]. However, for a fixed spatial mesh size Δx, a too long time integration will result in the accumulation of time discretization error for the Brownian paths, thus leading to the degeneracy of the numerical solutions as shown in our numerical experiments. Therefore, the choices for NT and Δx for our method are more complicated than that for the number of paths N, and have been tested, as discussed above, to give the 3% relative errors in our simulations.

The traditional Monte Carlo methods for computing high dimensional integrals has a $1/\sqrt{N}$ convergence rate where N is the number of samples in the simulation. However, in computing the path averages in the Feynman-Kac formula for the Neumann solution, the accuracy for the local time will also affect the overall accuracy of numerical methods. Regarding the former, Révész [9] proposed several approximations of the local time for 1-D Brownian motions with convergence rates ranging from $O(\Delta t^{1/4})$ to $O(\Delta t^{1/3})$. Such an analytical result is expected to hold in higher dimensional Brownian motions. As such, we expect the overall convergence rate for our Neumann solution will be limited by that of the local time.

In Table 1, we have included the relative errors of the Neumann solution monitored along a circle and a line segment in terms of the number of paths N. For all simulations, $\Delta x = 5 \times 10^{-4}$ and the strip width ε is chosen to be $3\Delta x$. The numerical results show that the convergence rate is around $O(1/N^{\alpha}), \alpha = 0.29$, which is less than the $O(1/\sqrt{N})$ convergence rate of Monte Carlo integrations. Meanwhile, the relative error of 2.87×10^{-2} for the Neumann solution is approximately at the same order of $\Delta t^{1/4} = 1.68 \times 10^{-2}$ for $\Delta t = (\Delta x)^2/3, \Delta x = 5 \times 10^{-4}$, reflecting the error estimate of local time in [9].

Table 1: Convergence rate of relative errors as $O(1/N^{\alpha})$ for the Neumann solution in a cube where $\Delta x = 5 \times 10^{-4}, \varepsilon = 3\Delta x$.

	$NT = 2.5 \times 10^4$	α	$NT = 2.9 \times 10^4$	α
N	errors on the line		errors on the circle	
2×10^2	0.2316		1.0158	
2×10^3	0.0364	0.37	0.4395	0.52
2×10^4	0.0345	0.15	0.0717	0.59
2×10^5	0.0178	**0.29**	0.0287	**0.39**

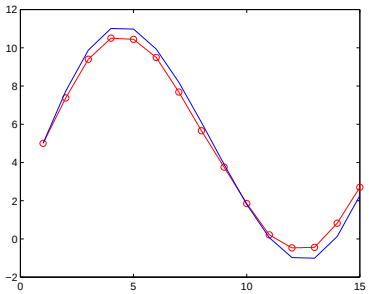

(a) $\varepsilon = 3\Delta x$, Err = 10.50%, NT = 2.7×10^4

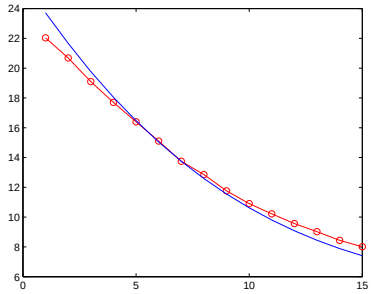

(b) $\varepsilon = 3\Delta x$, Err = 3.83%, NT = 2.4×10^4

Figure 8: Cubic domain: number of paths $N = 2 \times 10^5$. (Left) Solution on the circle; (right) solution on a line segment.

In the rest of the numerical tests, we will set $\Delta x = 5e - 4$ and the number of path $N = 2 \times 10^5$ but change NT by different boundaries.

- Spherical domain

The unit ball is centered at the origin. Similar numerical results are obtained as in the case of the cube domain. Here, the reflected points of Brownian path are the intersection of the normal and the domain. Though both Fig.10(a) and Fig.10(b) shows little deviation in the middle, the overall approximation are within an acceptable relative error less than 5.26%.

- Ellipsoidal domain

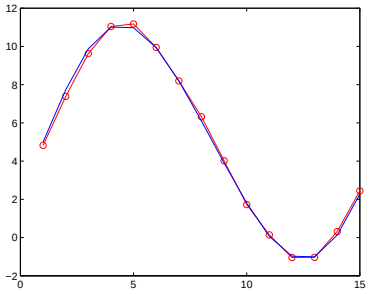

(a) $\varepsilon = 3\Delta x$, Err = 2.87%, NT = 2.9×10^4

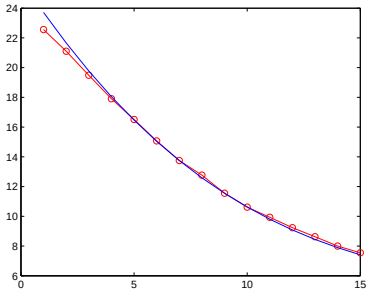

(b) $\varepsilon = 3\Delta x$, Err = 1.78%, NT=2.5×10^4

Figure 9: Cubic domain: number of paths $N = 2 \times 10^5$. (Left) Solution on the circle; (right) solution on a line segment.

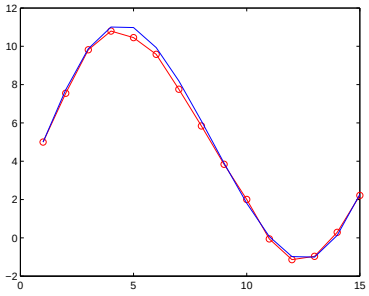

(a) $\varepsilon = 3\Delta x$, Err = 5.26%, NT = 5×10^4

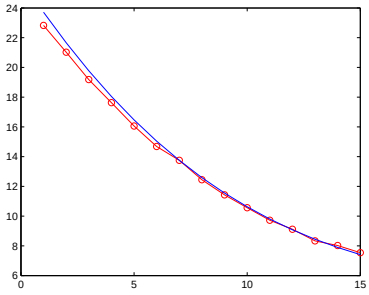

(b) $\varepsilon = 3\Delta x$, Err = 2.00%, NT = 4.5×10^4

Figure 10: Spherical domain: number of paths $N = 2 \times 10^5$. (Left) Solution on the circle; (right) solution on a line segment.

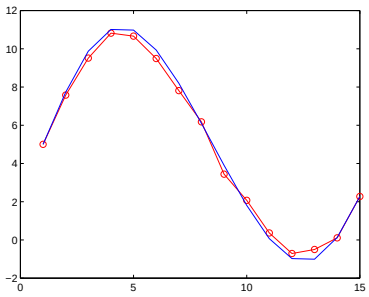

(a) $\varepsilon = 3\Delta x$, Err = 8.85%, NT = 5.025×10^4

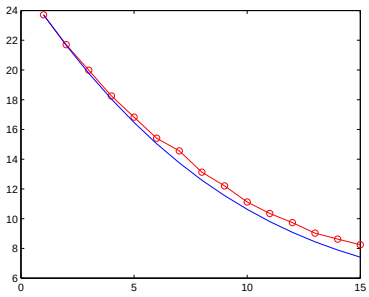

(b) $\varepsilon = 3\Delta x$, Err = 1.69%, NT = 4.525×10^4

Figure 11: Ellipsoidal domain: number of paths $N = 2 \times 10^5$. (Left) Solution on the circle; (right) solution on a line segment.

We use the ellipsoid with axis lengths $(3,\ 2,\ 1)$ centered at the origin. Δx remains to be $5e-4$. The numerical results (Fig.11) for circle are less accurate than for the cubic and spherical domains. A possible reason is as follows. An ellipsoid has "corners" around the longest axis if the lengths of three axis are not the same. When the initial point of the Brownian particle is far away from the "corners", the Brownian paths have a smaller probability to run into the regions close to those "corners". This implies that a large number of sampled paths starting at those points may stay away from the "corners", which may undermine the calculation accuracy of $u(x)$ since $u(x)$ is the weighted average over of Neumann data at hitting positions of RBM on the boundary. While the numerical solutions along the line segment show better accuracy.

- Non-convex and non-smooth domain

A non-convex domain in R^3 is constructed by rotating the profile of the function $y = 2x(x-1) - \sin(3\pi x)/8$ with respect to the x-axis with $x \in [0,1]$, as shown in Fig.12. This domain is not smooth as two pointed tips exist at the extreme values of x, i.e. $[0,0,0]$ and $[1,0,0]$, respectively. However, the probability of RBM hitting those two tips is zero. For

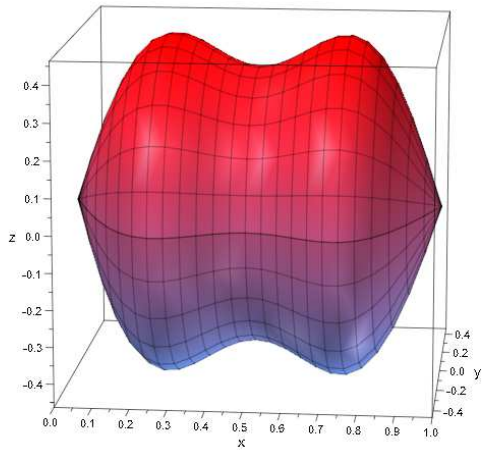

Figure 12: Non-convex domain by rotating $2x(x-1)-\sin(3\pi x)/8$ along x-axis with $x \in [0,1]$.

the sake of computing the RBM paths, the normals at $[0,0,0]$ and $[1,0,0]$ are set to be unit vector along negative and positive x-axis, respectively. The numerical results along a line segment connecting $[0.3,-0.1,-0.2]$ and $[0.75,0.2,0.4]$ with 15 evenly distributed points are displayed in Fig.13. Despite the non-convexity and non-smoothness of the domain, our numerical method is shown to work with a very small average relative error 0.56% with $N = 2\times 10^5$ sample paths, each of length $NT = 2.5\times 10^4$.

- Exterior Neumann problem for a domain of multiple spheres

Now we consider the exterior Neumann problem of a domain whose boundary is formed by multiple spheres, as shown in Fig.14. Thirty small hemispheres, with varying radii ranging from 0.12 to 0.18, are superimposed on the surface of a unit sphere with no overlapping between the small spheres. The solution domain is formed by the big sphere and thirty small hemispheres. We will calculate the potential on the boundary for the exterior Neumann problem of this domain. Using the Feynman-Kac formula, we can find the potential

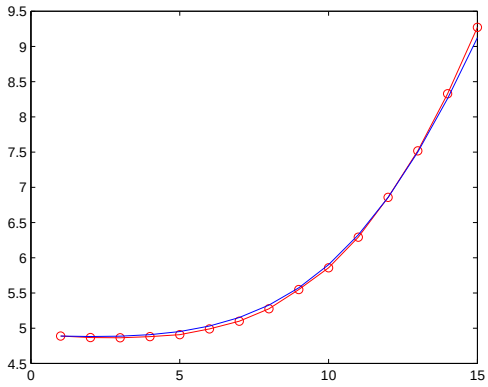

Figure 13: Non-convex domain: $\Delta x = 4.5e-4$, ε = $3\Delta x$, Err = 0.56%, N=2×10^5, NT = 2.5×10^4.

at any single point within the domain. By our algorithm, we can simply place the point on the boundary and start the reflecting Brownian path from that point. Solutions at fourteen points with ten points on the unit sphere and four points on the small hemispheres are calculated. For this case, the analytical solution is set to be $10/\sqrt{(x-0.5)^2+y^2+z^2}$. Fig.15 shows the satisfactory results of the algorithm on the boundary with a relative error around 2%. Note that for the exterior problem, the Brownian path may go to infinity so a large boundary is needed to mark the paths considered to be far away from the domain boundary, namely, escaping to infinite, and here a much larger sphere with radius $20R(R=1)$ is chosen. Finally, the number of Monte Carlo path samples is taken to be 2×10^4, giving the obtained results.

5.4.2 Some numerical issues and comparison with exisiting MC and grid-based methods

- Calculation of distance and parallel implementation

It is clear that the calculation of the distance to the boundary accounts for a large portion

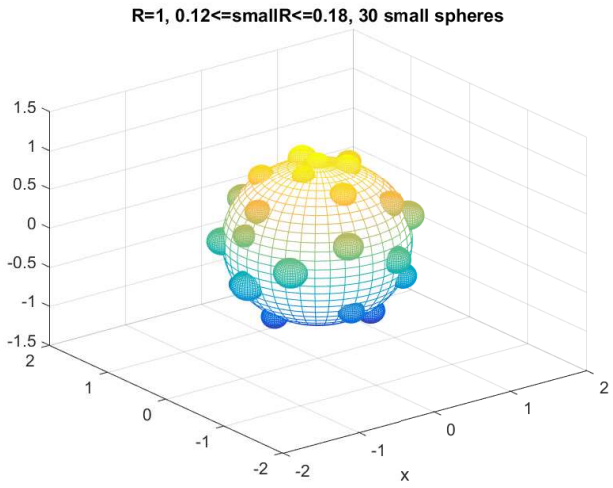

Figure 14: A domain with a boundary formed by multiple small hemispheres and a unit sphere.

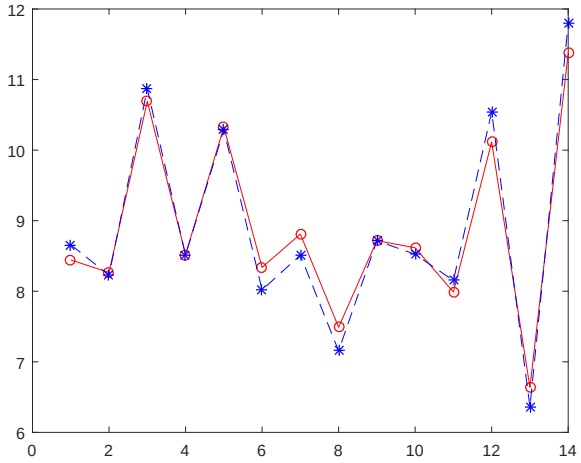

Figure 15: Exterior Neumann problem for the domain in Fig.13: exact potentials (asterisks) and numerical solutions (circles) on the boundary with a relative error of 2.31%. $\Delta x = 5 \times 10^{-4}$, $\varepsilon = 3\Delta x$, N=2×10^4, NT = 5×10^4.

of computing time for the WOS algorithm. In the multiple-spheres example, it takes a little time to find the closest point on the boundary by looping over all the thirty small hemispheres. But, consider the case of a boundary formed by many more small spheres, e.g. 1000 spheres, it will be time-consuming to calculate the distance. However, if the radii of the small spheres is small, some existing packages, for instance nanoflann library [47], can be used to speed up the closest-point query. One may find the applications in calculating the electric properties of materials of special shapes [65]. In the case of general domains, a regular Cartesian mesh covering the whole domain can be used to facilitate the calculation. As the signed distance function is a smooth function of position if it is given a negative value of the absolute distance outside the domain, we can pre-calculate the signed distance function at the regular mesh points, and the distance for any interior point to the boundary can be approximated accurately by appropriate high order interpolations of the distance function values on the mesh points. This greatly reduces the computing time at each step of the WOS algorithm. Also, as our algorithm requires the exact reflecting point on the boundary when the path exits the domain, a Newton root-finding method will be used to locate the nearest point on the boundary along the inward normal.

The MC approach of our method is intrinsically parallel as paths initiating from the location where the PDE solution is sought after are independent, a large number of paths can be sampled simultaneously on a multiple-core/nodes computer in a perfectly parallel manner and only at the end of the simulation the data is collected to compute the average in the Feynman-Kac formula.

- Memory use and CPU time for sampling pathes

For each sample path, the hitting locations and corresponding local time are recorded to evaluate the average of contributions of each path. Therefore, the memory storage required for the algorithm is $O(N \cdot NT)$ given N paths, each of length NT. If distance functions are pre-calculated, as needed for a domain of general shape, additional memory of $O(N_1^3)$ (N_1 be the number of subdivision along each dimension of the domain), is needed to store the distance function values on the mesh. The CPU time of the algorithm mainly arises from the calculation of the distance to the boundary and the reflecting points. For cube and sphere domains, it is trivial and thus quick to compute. For general domains, one should take into account of CPU time spending on the Newton method used to find the reflecting points on the boundary. Naturally, the overall CPU time also depends on the number of sample paths, length of each path in proportion.

- Comparison to an existing MC for the Neumann problem

In [20], the diffusion process generated by the Laplace operator is approximated by a transport process depending on a small parameter $\varepsilon \geq 0$. Then the original problem is reduced to a transport problem with a simple algorithm, since the particle moves in a given direction at a given speed until the next collision which changes its direction. This kinetic approximation was initially adopted to simulate diffusions with piecewise constant coefficients locally to treat the interface [62] in R^d. Satisfactory results for the Dirichlet boundary problem has also been acheived. Later [20] took advantage of the idea to treat the reflecting Brownian process.

A Monte Carlo method for the Neuman problem of the Poisson equation was proposed in [20] where WOS method was also used to simulate Brownian motions. The main difference

from the algorithm in this paper is about how to treat the Brownian paths once they enter the ε-layer of the boundary. In [20], once the path enters the ε-layer, the path is then projected onto the boundary, say at (x,y). And, in order to continue the walk back into the domain, with the help of the Neumann data $\phi(x)$, a Taylor expansion for the PDE solution is used to relate the solutions at a grid point of a local regular mesh of size h inside the domain, say $(x+h,y)$, and at the boundary in the form of $u(x,y) = u(x+h,y) + 2h\phi(x)$. A randomization of this relation shows the score of the walk should be increased by an amount of $2h\phi(x)$ and the walk arrives at the new position $(x+h,y)$ inside the domain. Moreover, in order to introduce the elapsed time for each walk, a kinetic approximation of the diffusion operator by a neutron transport operator is used such that the new position of the walk can be at $(x+hv_x t_c, y+hv_y t_c)$, where (v_x, v_y) is the velocity of the walk, t_c is a small parameter, and $h^2 t_c$ will be the elapsed time to arrive this new position. A Taylor expansion of the solution will give a similar afore-mentioned relation, which indicates a different score increment $4\phi(x)h/\pi$. And, the motion of the walk continues until the pre-set truncation time of the path is reached.

In terms of complexity and memory usage, the MC algorithm of [20] is similar to the method introduced in this paper as it only needs to record the locations when the Brownian path enter ε-layer and the projected position onto the boundary and the times (or stepsizes) at each walk step.

However, there is one difference in the way when a path is considered having hit the boundary and then reflected back into the domain. In our algorithm, the path has to "physically" cross the boundary before it is treated as a RBM path. In the approach of [20], once a path enters the ε-layer, it is then considered as a RBM path, as a result, this ap-

proach may treat a Brownian path which enters the layer, then leaves it without hitting the boundary for a while, also as behaving as a RBM path, in fact the local time increment for this path before it re-enters the ε-layer should be zero. The effect of this happening to the averages in the Feynman-Kac formula is not clear and should be investigated in relation to the thickness of the ε-layer .

- Comparison to grid-based method

Comparing to grid based method such as finite element method with a mesh size $\Delta x = \Delta y = \Delta z = \frac{L}{N}$ for a cube of $[0,L]^3$, an unstructured mesh as in a general domain will require $O(N^3)$ memory while the generation of the mesh itself will also take large amount of CPU time. An iterative solver such as GMRES or conjugate gradient will take $O(pN^3)$ flops for p-iterations. The main difference is that the grid-based method has to find the solution in the whole solution domain while the Monte Carlo method allows the solution at one single point. For the Monte Carlo method used in this paper, to find the solution at one single point, we only need to record the times and locations where the reflecting Brownian path hits the boundary for each of the N and no mesh generation and linear solver is required either.

5.4.3 Robin Boundary Problem

To guarantee the convergence of the numerical solutions to the analytical ones, we choose $c(X_t)$ to be negative functions so that the Robin boundary problem has a unique solution (when $c(X_t)$ is positive, the uniqueness is not guaranteed). Two cases are considered, $c(X_t) = -1$ and $c(X_t) = -|x|$ and two test points (0.1,0,0), (0.4,0.4,0.6) are selected to check accuracy of our numerical method described earlier. Below shows the results for

cubic, spherical and ellipsoidal domains respectively.

- Example 1 $\quad c(X_t) = -1$

Table 2: Cube domain when $c(X_t) = -1$

Point	N	NT	Δx	$\tilde{u}$	u	|Err|
(0.1,0,0)	2×10^5	3×10^4	0.002	4.7994	5	4.01%
(0.4,0.4,0.6)	2×10^5	4.2×10^3	0.0005	23.4916	23.7125	0.93%

Table 3: Spherical domain when $c(X_t) = -1$

Point	N	NT	Δx	$\tilde{u}$	u	|Err|
(0.1,0,0)	2×10^5	7×10^3	0.003	4.8322	5	3.35%
(0.4,0.4,0.6)	2×10^5	6×10^3	0.0005	23.7618	23.7125	0.21%

Table 4: Ellipsoidal domain when $c(X_t) = -1$

Point	N	NT	Δx	$\tilde{u}$	u	|Err|
(0.1,0,0)	2×10^5	2.5×10^4	0.003	5.0373	5	0.75%
(0.4,0.4,0.6)	2×10^5	4.5×10^3	0.0005	23.5394	23.7125	0.73%

- Example 2 $\quad c(X_t) = -|x|$

Table 5: Cube domain when $c(X_t) = -|x|$

Point	N	NT	Δx	$\tilde{u}$	u	|Err|
(0.1,0,0)	2×10^5	3.5×10^4	0.003	4.8797	5	2.41%
(0.4,0.4,0.6)	2×10^5	5.5×10^3	0.0005	24.0368	23.7125	1.37%

Table 6: Spherical domain when $c(X_t) = -|x|$

Point	N	NT	Δx	$\tilde{u}$	u	|Err|
(0.1,0,0)	2×10^5	2.7×10^4	0.003	4.8036	5	3.93%
(0.4,0.4,0.6)	2×10^5	7×10^3	0.0005	24.4202	23.7125	2.98%

Table 7: Ellipsoidal domain when $c(X_t) = -|x|$

Point	N	NT	Δx	$\tilde{u}$	u	|Err|
(0.1,0,0)	2×10^5	1.2×10^4	0.003	4.9492	5	1.02%
(0.4,0.4,0.6)	2×10^5	5×10^3	0.0005	23.2270	23.7125	2.05%

The two test points are far away from each other with (0.1,0,0) being closer to the origin and (0.4,0.4,0.6) closer to the boundary. Table 2-7 display two different selections of Δx for the two points under different domains and $c(X_t)$. Meanwhile, the length of path NT of the first point is longer than that of the second one under the two selections fo Δx. Physically, it reveals that the Browian paths should walk a much longer distance for the first point in the space. If the same Δx =5e-4 was employed to (0.1,0,0), it may require an even longer path to reach the same accuracy that we've already gained in the tables. Note that, when

NT gets longer the error of boundary local time accumulates simultaneously, which may undermine the accuracy of approximations. This should be an interesting topic to explore for our future work.

CHAPTER 6: ELECTRIC IMPEDANCE TOMOGRAPHY

With both Neumann and Robin boundary problems explored, we will consider applications of the boundary value problems in Electric Impedance Tomography (EIT).

6.1 Introduction to Electric Impedance Tomography

Electrical Impedance Tomography (EIT) is a non-invasive medical imaging technique in which an image of the electrical properties (conductivity or permittivity) of part of the body is inferred from surface electrode measurements. It has the advantages over other current techniques like X-rays and requires no exposure to radioactive materials. Applications include detection of breast cancer, pulmonary emboli, blood clots and impaired gastric emptying. Essentially, only by surface measurements, internal electric conductivity and permitivity are desired to be recovered as an image across the human body. For instance, the electric conductivity of malignant tumor, high-water-content tissue, is one order higher than that of the normal (fat) tissue, which allows one to identify the potential diseases and locations through the constructed image over the body [66].

EIT is also a useful tool in other fields such as geophysics, environmental sciences and nondestructive testing of materials. For instance, it is able to locate the underground mineral deposits, detect leaks in underground storage tanks and monitor flows of injected fluids into the earth for extraction or environmental cleaning. Moreover, EIT can detect the the corrosion or defects of construction material and machine parts [66][48] when invasion

testing is not possible or destructive.

The mathematical model or conductivity equation reads

$$\nabla \cdot \gamma \nabla u = 0 \tag{6.1.1}$$

where γ is the electric conductivity varying at different locations. Only isotropic conductivities are considered in our work, so no permittivity appears.

Researchers are concerned with how to work out the conductivity inside an object if only some boundary measurements are available. It is well known that this inverse problem is nonlinear, unstable and intrinsically ill-posed [48].

Theoretically speaking, complete boundary measurements indeed determine the conductivity in the interior uniquely [55] [56], yet only limited number of electrodes and current patterns are available in practice for measurements. More details and discussions of the theoretical inverse problem is followed in the next section.

6.2 Forward Problem and Inverse Problem

6.2.1 Complete Electrode Model

To obtain the surface measurements, alternating currents are applied on different combination of electrodes attached on the surface of the object. Then the resulting voltages will be measured with the same electrodes. An estimate of the internal conductivity distribution over the object is expected to be reconstructed by using those voltage measurements. In other words, the prerequisite of an accurate EIT reconstruction is to have a forward model capable of predicting the voltages on electrodes. There have been developed several mathematical models to compare with the experimental data. As a matter of fact, continuum

model, gap model, shunt model and complete models are the most commonly used in modelling electrodes. Among all, the complete model was shown to be capable of predicting the experimentally measured voltages to withing 0.1% on the electrodes and the existence and uniqueness were proved in [58]. Next we will introduce the complete model in this section and it is chosen to be our forward problem in approximating the electric fields.

- Complete Electrode Model (CEM)

Suppose the domain of the object is Ω and L electrodes $E_i, i = 1, ..., L$ are attached to the boundary of the domain. The complete electrode model assumes the following

$$\nabla \cdot \gamma \nabla u = 0, \quad in\ \Omega \tag{6.2.1a}$$

$$\int_{E_l} \gamma \frac{\partial u}{\partial n} dS = I_l, \quad l = 1, 2, ..., L \tag{6.2.1b}$$

$$\gamma \frac{\partial u}{\partial n} = 0, \quad \text{off } \cup_{l=1}^{L} E_l \tag{6.2.1c}$$

$$u + z_l \gamma \frac{\partial u}{\partial n} = U_l \quad \text{on } E_l, \quad l = 1, 2, ..., L. \tag{6.2.1d}$$

$$\tag{6.2.1e}$$

(6.2.1a) describes the change of electric potential in the interior of the object where γ is the conductivity or inverse of the resistivity. It was derived from Maxwell equations by neglecting the time-dependence of the alternating current and assuming the current source inside the object to be zero [58]. Both (6.2.1b) and (6.2.1c) show the knowledge of current density on the boundary and (6.2.1d) takes account of the electrochemical effect by introducing z_l as the contact impedance or surface impedance which quantitatively characterizes a thin, highly resitive layer at the contact between the electrode and the skin, which

causes potential jumps according to the Ohms law. It should be noted that, the regularity of potential decreases as the contact impedance approaches zero [62], which becomes a huge hindrance since usually good contacts (or small contact impedance) are desired in practice.

6.2.2 Calderón Problem

Calderón Problem Let Ω be a bounded domain in $R^n, n \geq 2$, with Lipschizian boundary $\partial\Omega$, and γ be a real bounded measurable function in Ω with a positive lower bound. Consider the differential operator

$$L_\gamma(w) = \nabla(\gamma\nabla w) \tag{6.2.2}$$

acting on $H^1(\Omega)$ and the quadratic form $Q_\gamma(\phi)$, where the functions in $H^1(R^n)$ defined by

$$\begin{aligned} Q_\gamma = \int_\Omega \gamma(\nabla w)^2 dx, w \in H^1(R^n), w|_{\partial\Omega} = \phi \\ L_\gamma w = \nabla\cdot(\gamma\nabla w) = 0 \ in \ \Omega. \end{aligned} \tag{6.2.3}$$

The problem is then to decide whether γ is uniquely determined by Q_γ and to calculate γ in terms Q_γ if γ is truly determined by Q_γ. Put it in another way, is the map

$$\Phi : \gamma \to Q_\gamma \ \text{ injective?} \tag{6.2.4}$$

As discussed in the begining of this chapter, one would like to identify the conductivity through the surface electrode measurements without penetrating Ω. Within the context of physics, $Q_\gamma(\phi)$ represents the power necessary to maintain an electrical potential ϕ on $\partial\Omega$. Calderoń showed that Φ is analytic if $\gamma \in L^\infty(\Omega)$ and $d\Phi|_{\gamma=const}$ is injective. He also proved that Q_γ determines Γ when γ is sufficiently close to a constant with an error estimate.

Many authors have made contributions to the problem under various assumptions. Kohn

and Vogelius [55] provided positive an answer to the determination of the conductivity and all of its derivatives at the boundary. Sylvester and Uhlmann [56] proved uniqueness for C^2 conductivities in the plane. While Brown [63] relaxed the regularity of the conductivity to $3/2+\varepsilon$ derivatives.

We may treat Calderón Problem from another perspective. To be more specific, knowing $Q_\gamma(\phi)$ for each $\phi \in H^{1/2}(\Gamma)$ is equivalent to the knowledge of "Dirichlet-to-Neumann" data. In fact, by the Green's identity

$$\int_\Omega [v\nabla\cdot(\gamma\nabla u)+\nabla v\cdot\gamma\nabla u]\,dx = \int_\Gamma v\cdot\gamma\frac{\partial u}{\partial n}dS. \tag{6.2.5}$$

If $v=u$ above, then

$$\int_\Omega \gamma|\nabla u|^2 dx = \int_\Gamma \phi\cdot\gamma\frac{\partial u}{\partial n}dS, \tag{6.2.6}$$

where the left-hand side of (6.2.6) is exactly $Q_\gamma(\phi)$ and the other side is Neumann values given Dirichlet conditions on the boundary. Thus, the **Calderón Problem** can be restated as whether γ is uniquely determined by the "Dirichlet-to-Neumann" mapping on the boundary. The map tells us how the boundary potential determines the current flux across the boundary [64]. Furthermore, a "Robin-to-Neumann" (or voltage-to-current) mapping is essentially equivalent to a "Dirichlet-to-Neumann" mapping through a close look at (6.2.1d). Given a full Robin-to-Neumann map $R_{z_l,\gamma}:\phi\to\gamma\nabla u|_{\partial\Omega}$, it uniquely determines z_l and thus equivalent to the Dirichlet-to-Neuman map. Under such circumstances, uniqueness of solutions to the inverse conductivity problem was proved by Astala and Päivärinta [51] without any regularity imposed on the boundary given a bounded measurable conductivity in two dimensions. In three dimensions, Haberman and Tararu [64] confirmed the answer

for C^1 conductivities and Lipchitz conductivities close to identity.

Various numerical algorithms to reconstruct the conductivity on the boundary have been proposed and fall into two categories, noniterative and interative methods. Noniterative methods were developed based on the assumption that the conductivity does not differ too much from a constant. Calderón [49] proved that the map in (6.2.4) is injective when γ is close to a constant in a sufficiently small neighborhood, and thus an approximation formula was given to reconstruct the conductivity. Barber-Brown backprojection method [54] gave a crude approximation to the conductivity increment $\delta\gamma$ based on inverse of the generalized Radon transform, which works best for smooth $\delta\gamma$ or $\delta\gamma$ whose singularity is far from the boundary. For the L-electrode system, Noser algorithm minimizes the sum of squares error of the voltages on the electrodes by taking one step of a regularized Newton's method. While the iterative methods are devoted to minimize different regularized least squares functionals like Tikhonov regularization [57] method and totoal variation method [52] where iterative gradient-based optimization algorithms are commonly used.

6.2.3 Robin-to-Neumann Map

The Robin-to-Neumann map may also be called a voltage-to-current map due to its equivalence to the Dirichlet-to-Neumann map. In the inverse problem, iterative algorithms usually require solving the forward problem at each iteration numerically then the computation time accumulates excessively for the commonly used FEM method.

One possible way to improve the efficiency would be to develop a probabilistic estimator of the voltage-to-current map. The main advantage of the method lies in the prevailing multicore computing. Maire and Simon [62] proposed a so-called partially reflecting random

walk on spheres algorithm to compute voltage-to-current map in a parrallel manner, which is also specially efficient when only solutions at only a few points are desired. For the Dirichlet boundary problem, it is well known that killed Brownian motion is the stochastic process that governs the differential operator. Instead, in the mixed boundary situations, the partially reflecting Brownian motion comes into play in preventing the path running out of the domain by either absorptioin or instantenous reflection. Simulation of absorption is much easier to take care of comparing to that of reflection which usually needs special techniques like local finite difference discretizations. Various schemes of first order or second roder schemes have been proposed and analyzed [20][46]. Maire and Simon also proposed a similar approach involving second order space discretization scheme. A variance reduction technique was introduced as well to improve the efficiency and accuracy of the method.

In our work, we aim to find a probabilistic solution to the voltage-to-current map by directly simulating the reflecting Brownian motion paths. More precisely, the calculation of the boundary local time is treated explicitly in details and coupled with the Feynman-Kac type representation, then the voltages are obtained numerically on the boundary and by simple integrations the currents can be worked out.

The rest of the chapter is devoted to the realization of voltage-to-current map using an example in 3D.

6.3 Computational Procedure

Again, in medical applications, limited electrodes are attached to human body to get measurements. Our numerical test was performed based on a unit spherical model, see Fig.

17. Eight electrodes are imposed on the boundary and the centers of the electrodes all lie on the $y-z$ plane with radius 0.2.

Consider the Laplace equation with both Neumann and Robin boundary problem

$$\begin{cases} \Delta u = 0 \quad \text{in } \Omega \\ z_l \nabla u + u = \phi(x) =: cos(4\theta) \quad \text{on } E_l, \text{ l=1,...,8} \\ \dfrac{\partial u}{\partial n} = 0 \quad \text{D=off} \cup_{l=1}^{8} E_l \end{cases} \tag{6.3.1}$$

where z_l is a constant bounded by 0 and 1. Here we choose z_l be 0.5 as an example.

In this section, we will describe two methods to find a Robin-to-Neumann mapping.

A. Direct WOS sampling on the boundary

In Chapter 5, the numerical results are shown for the multisphere boundary formed by multiple small hemispheres and a unit sphere. The test points are chosen on the boundary so that the Brownian path starts on the boundary by WOS sampling. Now the same idea is adopted but for an interior problem with mixed boundary conditions. In other words, we aim to find the potentials on the electrodes through numerical method described in Chapter 5, then by Robin boundary conditions the Neumann values are automatically known.

B. Local boundary integral equation

It is also possible to consider solving local boundary integral equations for the Neumann values around each electrode. The main construction follows from [27]. To illustrate the method, a sphere centered at x with radius r is superimposed on an arbitrary bounded domain (Fig.16). Then the region bounded by the sphere and the big domain formed a new domain Ω_x with two boundary surfaces S and Γ.

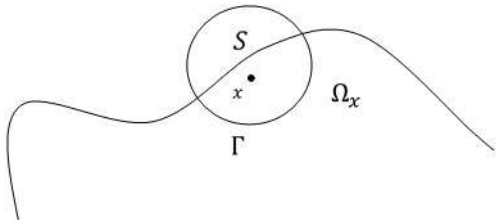

Figure 16: Local boundary integral integration domain

The second Green's identity shows

$$\int_{\Omega_x} (u(y)\Delta G(x,y) - G(x,y)\Delta u(y))\, dy = \int_{\Gamma\cup S} \frac{\partial G(x,y)}{\partial n_y} u(y) dS_y - \int_{\Gamma\cup S} G(x,y) \frac{\partial u(y)}{\partial n_y} dS_y. \tag{6.3.2}$$

When x approaches S from the interior of Ω_x,

$$-\frac{1}{2}u(x) = \int_{\Gamma\cup S} \frac{\partial G(x,y)}{\partial n_y} u(y) dS_y - \int_{\Gamma\cup S} G(x,y) \frac{\partial u(y)}{\partial n_y} ds_y, \tag{6.3.3}$$

or

$$\frac{1}{2}u(x) = -p.v. \int_{\Gamma\cup S} \frac{\partial G(x,y)}{\partial n_y} u(y) dS_y + \int_{\Gamma\cup S} G(x,y) \frac{\partial u(y)}{\partial n_y} ds_y. \tag{6.3.4}$$

Let $G(x,y)|_{y\in\Gamma} = 0$,

$$\frac{1}{2}u(x) = -p.v. \int_S \frac{\partial G(x,y)}{\partial n_y} u(y) dS_y - \int_\Gamma \frac{\partial G(x,y)}{\partial n_y} u(y) dS_y + \int_S G(x,y) \frac{\partial u(y)}{\partial n_y} dS_y. \tag{6.3.5}$$

Under the Robin boundary condition for u, $\frac{1}{2}\frac{\partial u(x)}{\partial n_x} + u = \phi(x)$,

$$\begin{aligned} \frac{1}{2}\left(-\frac{\partial u(x)}{2\partial n} + \phi(x)\right) = -p.v. \int_S \frac{\partial G(x,y)}{\partial n_y} \left(-\frac{\partial u(y)}{2\partial n_y} + \phi(y)\right) dS_y - \\ \int_\Gamma \frac{\partial G(x,y)}{\partial n_y} u(y) dS_y + \int_S G(x,y) \frac{\partial u(y)}{\partial n_y} ds_y. \end{aligned} \tag{6.3.6}$$

$$\frac{1}{4}\frac{\partial u(x)}{\partial n}+\frac{1}{2}p.v.\int_S \frac{\partial G(x,y)}{\partial n_y}\frac{\partial u(y)}{\partial n_y}dS_y+\int_S G(x,y)\frac{\partial u(y)}{\partial n_y}ds_y = p.v.\int_S \frac{\partial G(x,y)}{\partial n_y}\phi(y)dS_y+ \frac{1}{2}\phi(x)+\int_\Gamma \frac{\partial G(x,y)}{\partial n_y}u(y)dS_y. \tag{6.3.7}$$

The notation "p.v." in the above equations denotes the principle value of the integral when the singularity exists. Since it is merely weakly singular, a polar transform can be carried out to remove it easily.

If a boundary mesh is set up on S with mesh points $\cup_{i=1}^{N} x_i$, then for each x_i, we have one above equation and together a system of bounary integral equations is obtained. The solutions to the system will then give us the Neumann values.

Remark 6. The reference solutions are required for the whole spherical boundary to gauge the accuracy of the numerical approximations of potentials on S and Γ for method A and B respectively. While method A is more straightforward, no integral equations need to be solved. As long as the numerical approximations of potential are accurate, the resulting Neumann values should have the same accuracy. Method B involves singularies at the intersection of S and Γ which will result in large error around surrounding area. To overcome this, a radius larger than that of the electrode may be taken so that the local boundary integral equations will yield accurate Neumann values. We will implement method A and method B is similar except an extra local boundary integral equation system involved on Γ.

6.3.1 Reference solutions for unit sphere

- Mesh setup

Different boundary meshes are constructed on the electrode patches and off-electrode patch, see Fig.18 and Fig.19. Specifically, GMSH generates unstructured 3D meshes given

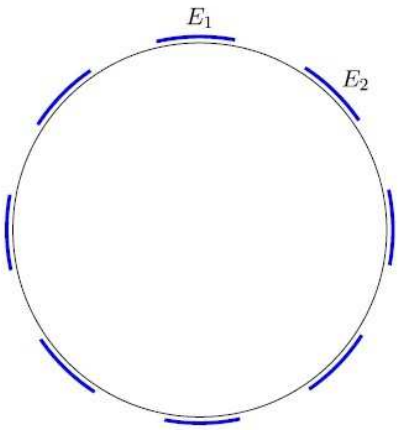

Figure 17: Limited electrodes model on unit sphere

a "size field" while the mesh on the electrode patches is clearly structured along the longitude and altitude and the mapping from the elemental triangle to the curved ones can be identified [45]. Thus global boundary integral equations can now be set up based on the two meshes.

Let Ω be the unit ball centered at the origin, and $\partial\Omega = D \cup E$, $E = \cup_{i=1}^{8} E_i$. Each electrode patch has the equal surface area as displayed in Fig.17.

The second Green's identity shows for any fixed $x \in \Omega$,

$$\int_{\Omega} (u(y)\Delta G(x,y) - G(x,y)\Delta u(y))\, dy = \int_{\partial\Omega} \frac{\partial G(x,y)}{\partial n_y} u(y) dS_y - \int_{\partial\Omega} G(x,y) \frac{\partial u(y)}{\partial n_y} dS_y. \tag{6.3.8}$$

When $x \to \partial\Omega$ from the interior, then

$$-\frac{1}{2}u(x) = \int_{\partial\Omega} \frac{\partial G(x,y)}{\partial n_y} u(y) dS_y - \int_{\partial\Omega} G(x,y) \frac{\partial u(y)}{\partial n_y} ds_y, \tag{6.3.9a}$$

$$-\frac{1}{2}u(x) = \int_{\partial\Omega} \frac{\partial G(x,y)}{\partial n_y} u(y) dS_y - \int_{E} G(x,y) \frac{\partial u(y)}{\partial n_y} ds_y, \tag{6.3.9b}$$

$$-\frac{1}{2}u(x) = \int_{\partial\Omega} \frac{\partial G(x,y)}{\partial n_y} u(y) dS_y - \int_{E} G(x,y) \left(\phi(y) - u(y)\right) / z_l ds_y, \tag{6.3.9c}$$

$$-\frac{1}{2}u(x) = \int_{\partial\Omega} \frac{\partial G(x,y)}{\partial n_y} u(y) dS_y - \frac{1}{z_l}\int_{E} G(x,y)\phi(y) dS_y + \frac{1}{z_l}\int_{E} G(x,y)u(y) dS_y, \tag{6.3.9d}$$

$$\tag{6.3.9e}$$

or

$$\frac{1}{z_l}\int_{E} G(x,y)\phi(y) ds_y = \frac{1}{2}u(x) + \int_{\partial\Omega} \frac{\partial G(x,y)}{\partial n_y} u(y) dS_y + \frac{1}{z_l}\int_{E} G(x,y)cu(y) dS_y. \tag{6.3.10}$$

where the condition (6.3.1) is used to deduce from (6.3.9a) to (6.3.9b). Therefore we obtain a global boundary integral equation for u. Build different meshes on D and E and let x move over all the mesh points, then through (6.3.10) we have a system for solving $u(x)$ on $\partial\Omega$, which means the reference potentials on the boundary can be obtained to make Monte Carlo simulations. Meanwhile, any reference potentials inside the domain can be achieved as well through

$$u(x) = \int_{\partial\Omega} G(x,y) \frac{\partial u(y)}{\partial n_y} dS_y - \int_{\partial\Omega} \frac{\partial G(x,y)}{\partial n_y} u(y) dS_y. \tag{6.3.11}$$

where $\frac{\partial u(y)}{\partial n_y}$, the Neumann values on the boundary, are automatically known once the reference potentials are found on the electrode patches based on the Robin conditions.

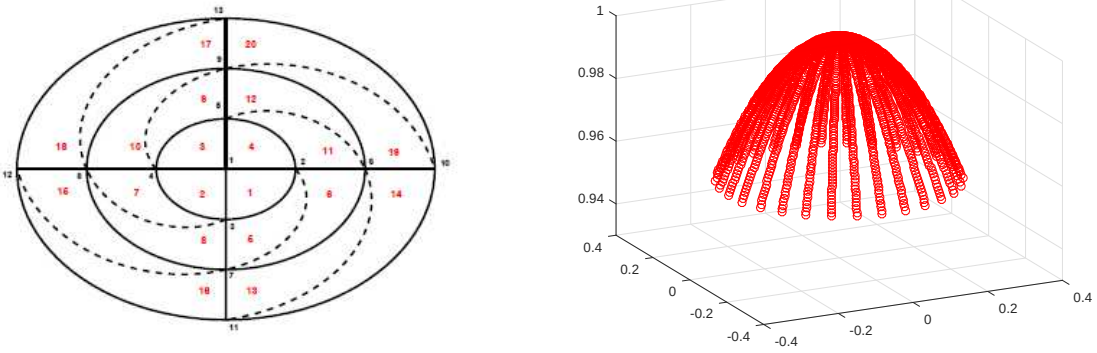

(a) Construction of curved triangles in 2D

(b) Mesh points of curved triangles

Figure 18: Curved triangles

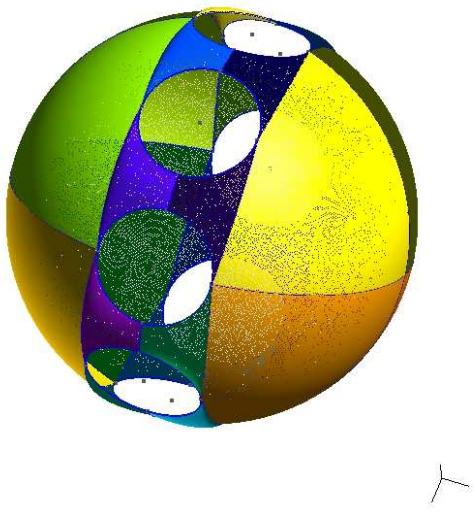

Figure 19: Boundary mesh generated by GMSH on off-electrode patch.

6.4 Numerical results

Since the contact impedance z_l variates from 0 to 1, we may take $z_l = 0.5$ as an example. Eight electrodes with radius $r = 0.2$ are superimposed on the $y-z$ plane. A close look at the boundary conditions in (6.3.1) reveals the discontinuity at the rims of all the electrodes. It is natural to enlarge the radius of mesh on E_i so that we may have an easy control over the mesh size for calculation. Assume the enlarged radius to be $r_e = 0.3$. Because of the discontinuity, we consider a graded mesh on the enlarged surface by introducing a layered structure, as Fig. 20 illustrates. There are four layers with the first from center to r_1, second from r_1 to r, third from r to r_2 and fourth from r_2 to r_e. Obviously, a dense mesh should be imposed around the rim ($r = 0.2$) of the electrode and that means both 2nd layer and 3rd layer should have a decreased mesh size towards $r = 0.2$. Further, a graded mesh also discretizes the first layer while an evenly distributed mesh is imposed on the fourth layer. And m_1, m_2, m_3 and m_4 are the number of divisions of altitude in each layer respectively. Here we take $m_1 = 20, m_2 = 16, m_3 = 16$ and $m_4 = 9$. The mesh size can be calculated through $dx \cdot \alpha^i, i = 0, ..., m_j - 1 (\alpha = 3/4, j = 1, 2, 3, 4)$. The number of divisions along longitude will be the same for each layer, i.e. $n = 120$. Fig.21 is the realization of the graded mesh on the north pole patch as discussed. The red points are the mesh points on the electrode (first two layers) and blue ones are off-electrode points on the rest two layers. We can clearly see the Meshes on $E_i, i = 2, ..., 8$ can be constructed similarly or obtained through rotation of that on E_1 along x-axis. Besides, the "size field" of GMSH is 0.012 on D which yields 88383 mesh points and 175530 triangle elements.

- Reference solutions

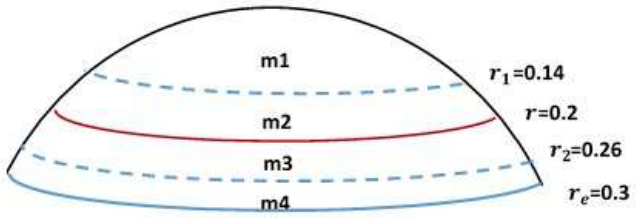

Figure 20: Graded mesh on electrode patches.

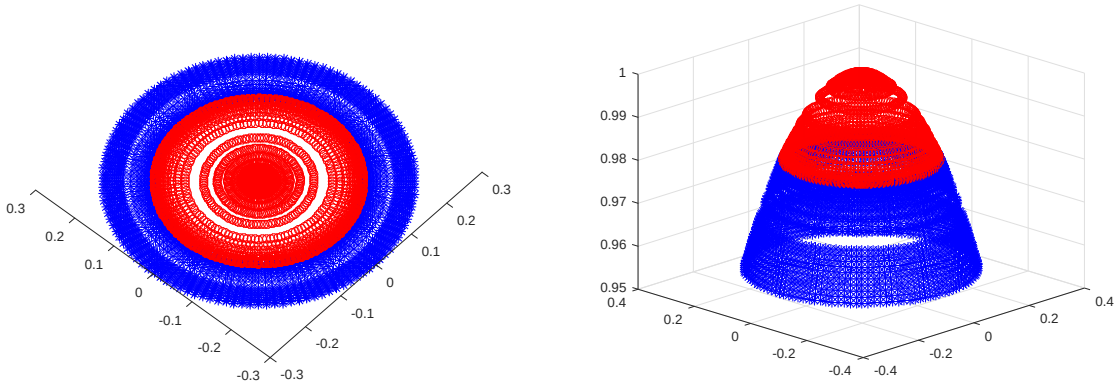

(a) View in 2D: Mesh points projected to x-y plane

(b) View in 3D

Figure 21: Mesh points on the north pole patch

We will show the result in terms of electrode currents. According to

$$J_l = \frac{1}{|E_l|}\int_{E_l} \frac{\partial u}{\partial n}|_{\partial D} d\sigma(x), \tag{6.4.1}$$

we have

Table 8: Reference currents on each electrode

Current	E_1	E_2	E_3	E_4
J_l^{ref}	1.3377346024	-1.3960453685	1.4543557058	-1.3960453502
Current	E_5	E_6	E_7	E_8
J_l^{ref}	1.3377346471	-1.3960453364	1.4543557459	-1.3960453565

A direct summation of J_l over eight electrodes yields the whole current to be **-7.10e-7** which is close to **0** as the conservation of charges condition suggests. Meanwhile the electrode currents show sysmetric patterns with respect to both y and z axis.

Based on the reference solution, we can now conduct Monte Carlo simulations and obtain the Neumann values through second equation of (6.3.1).

- Direct WOS sampling on the boundary

In Chapter 5, an example of direct sampling of exterior Neumann problem is given. We take the same idea here for the mixed boundary value problem. In other words, the Brownian path is initiated at the boundary and it will be pushed back if running out of the scope of domain otherwise it moves by the law of WOS described in Chapter 4. Under the mixed boundary conditions, the numerical solution to (6.3.1) is derived from (5.3.22) and thus

given by

$$\tilde{u}(x_0) = \sum_{i=1}^{N} \sum_{j:X_{t_j}\in E}^{NP} e^{\int_0^t c(X_{t_j})dL(t_j)} \frac{1}{z_l}\phi(X_{t_j})dL(t_j) \tag{6.4.2}$$

or

$$\tilde{u}(x_0) = \sum_{i=1}^{N} \sum_{j:X_{t_j}\in E}^{NP} e^{\sum_{k=0}^{j} c(X_{t_j})(n_k-n_{k-1})\frac{h^2}{3\varepsilon}} \frac{1}{z_l}\phi(X_{t_j})(n_j-n_{j-1})\frac{h^2}{3\varepsilon} \tag{6.4.3}$$

where x_0 is the initial point of Brownian motion X_t on the boundary.

Since the solution exists uniquely under the assumption of (6.3.1), at one single point we can definitely obtain an approximation . However, different initial points may require different length of path or even different Δx. It is still possible to try the same length of path NP for different points when they are close to each other. In our test, the mesh points on the north pole patch are divided into two groups and each group seems to gain high accuracy on average with the same length for its points respectively. Based on (6.4.1), Table 9 presents the numerical approximation and absolute error comparing to the reference current on north pole patch which was obtained earlier in Table 8. We do not list the numerical results for Neumann values here since there are too many points but the maximum error is small around 1.9% which is also demonstrated by the small error of current.

Table 9: Numerical approximation of the current on north pole patch

	J_1^{ref}	$\tilde{J}_1$	|Err|
Current	1.33773	1.33756	0.01%

With the numerical approximation of potentials on the boundary, the Neumann values are automatically known and thus a full Robin-to-Neumann mapping has been achieved over the whole boundary by conducting the same procedure at all the mesh points on dif-

ferent electrode patches. Therefore, we've found an effective way to identify the voltage-to-current mapping without constructing 3D mesh in the domain once the reference potentials are known on the boundary.

CHAPTER 7: CONCLUSIONS AND FUTURE WORK

In this study we have proposed numerical methods for computing the local time of reflecting Brownian motion and the probabilistic solution of the Laplace equation with the Neumann and/or Robin boundary condition. Without knowing the complete trajectories of RBM in space, we are able to use the WOS to sample the RBM and calculate its local time, based on which a discrete probabilistic representation (5.3.1) was obtained to produce satisfactory approximations to the solution of the Neumann/Robin problem at one single point. Numerical results validated the stability and accuracy of the proposed numerical methods.

In addition, random walk on a lattice was also investigated as an alternative way to sample RBM. However, numerical experiments show that the numerical results are inferior to those obtained by the WOS method. A possible reason is that formula (2.3.1) for the local time is valid for a smooth path while a random walk approximation of the the Brownian path contains inherent errors.

The local time can also be computed by a mathematically equivalent formula (2.3.3). Again the numerical results based on (2.3.3) are inferior to those obtained using the original limiting process of Lévy in [18] . We believe that this fact may result from the time discretization error of Brownian paths especially when long time truncation is employed in the probabilistic representation.

Various issues affecting the accuracy of the proposed numerical methods remain to be

further investigated, such as the number of random walk or WOS steps and the truncation of duration time T for the paths [20], the choice of the thickness for the ε-region, the size of Δx for the lattice, etc. Regarding the convergence rate of the proposed method, more theoretical work is needed on the exact rate of convergence. This will be helpful when the reference solutions of boundary value problems are difficult to obtain under special geometries.

For the purpose of application in material science, more flexible domains with local convexity will be considered as it relates to the calculations of electrical properties such as the conductivity of composite materials where the particle shapes plays an important role [41]. It should be noted that the distance calculation is the most time-consuming and for some special geometry data structures, algorithms are desired to quickly solve the closest-point queries [67].

REFERENCES

[1] A. Benchérif-Madani and E. Pardoux, *A probabilistic formula for a Poisson equation with Neumann boundary condition*, Stoch. Anal. Appl. 27 (2009), 739–746.

[2] I. Binder and M. Braverman,*The rate of convergence of the walk of sphere algorithm, Geometric and Functional Analysis*, Vol. 22, 558-587, 2012.

[3] M. Bossy, E. Gobet, and D. Talay, *Symmetrized Euler scheme for an efficient approximation of reflected diffusions*, Journal of applied probability 41.3 (2004): 877-889.

[4] G. A. Brosamler, *A probabilistic solution of the Neumann problem, Mathematica Scandinavica*, Vol. 38, 137-147, 1976.

[5] A. J. Chorin and O. H. Hald, *Stochastic tools in mathematics and science*, Dordrecht: Springer, Vol. 1, 2009.

[6] K. L. Chung and R. J. Williams,*Introduction to Stochastic Integration*, Progress in Probability and Statistics, Vol. 4, 1983.

[7] K. L. Chung, *Green, Brown, and probability*, Singapore: World scientific, 1995.

[8] C. Costantini, B. Pacchiarotti, and Flavio Sartoretto, *Numerical approximation for functionals of reflecting diffusion processes*, SIAM Journal on Applied Mathematics 58.1 (1998): 73-102.

[9] M. Csörgő and P. Révész , *Three Strong Approximations of The Local Time of a Wiener Process and Their Applications to Invariance*, North-Holland, 1984.

[10] F. Fogolari, A. Brigo, and H. Molinari, *The Boltzmann equation for biomolecular electrostatics: a tool for structural biology*, J. Mol. Recognit., Vol. 15, 377- 392, 2002.

[11] M. Freidlin, *Functional Integration and Partial Differential Equations*, Princeton University Press, 1985.

[12] A. Friedman, *Stochastic differential equations and applications*, Dover publication, 2006.

[13] J. A. Given, Chi-Ok Hwang and M. Mascagni, *First-and last-passage Monte Carlo algorithms for the charge density distribution on a conducting surface*, Physical Review E 66, 056704, 2002.

[14] (Elton) P. Hsu, *"Reflecting Brownian motion, boundary local time and the Neumann problem"*, Dissertation Abstracts International Part B: Science and Engineering[DISS. ABST. INT. PT. B- SCI. ENG.], Vol. 45, No. 6, 1984.

[15] G. J. Jiang and J. L. Knight, *A nonparametric approach to the estimation of diffusion processes, with an application to a short-term interest rate model*, Econometric Theory, 13(05), pp. 615-645, 1997.

[16] I. Karatzas and S. E. Shreve, *Brownian motion and stochastic calculus*, Springer-Verlag New York Inc., 1988.

[17] F. C. Klebaner, *Introduction to Stochastic Calculus with Applications*, Imperial College Press, 2001.

[18] P. Lévy, *Processus Stochastiques et Mouvement Brownien, Gauthier-Villars*, Paris, 1948.

[19] P. L. Lions and A. S. Sznitman, *Stochastic differential equations with reflecting boundary conditions*, Comm. Pure Appl. Math., 37 (1984), pp. 511-537.

[20] S. Maire and E. Tanré, *Monte Carlo approximations of the Neumann problem*, Monte Carlo Methods and Applications 19.3 (2013): 201-236.

[21] J. P. Morillon, *Numerical solutions of linear mixed boundary value problems using stochastic representations*, Int. J. Numer. Meth. Engng., Vol. 40, 387-405, 1997.

[22] P. Mörters and Y. Peres, *Brownian motion*, Cambridge University Press, Vol. 30, 2010.

[23] M. E. Müller, *Some continuous Monte Carlo methods for the Dirichlet problem*, The Annals of Mathematical Statistics, Vol. 27, No. 3, 569-589, 1956.

[24] K. K. Sabelfeld and N. A. Simonov, *Random walks on boundary for solving PDEs*, Walter de Gruyter, 1994.

[25] Y. Saisho, *Stochastic differential equations for multidimensional domain with reflecting boundary*, Probab. Theory Related Fields, 74 (1987), pp. 455-477.

[26] J. E. Souza de Cursi,*Numerical methods for linear boundary value problems based on Feynman-Kac representations*, Mathematics and Computers in Simulation, Vol. 36, No. 1, 1-16, 1994.

[27] C. Yan, W. Cai, and X. Zeng, *A parallel method for solving Laplace equations with Dirichlet data using local boundary integral equations and random walks*, SIAM J. Scientific Computing, Vol. 35, No. 4, B868- B889, 2013.

[28] A.V. Skorokhod, Stochastic equations for diffusion processes in a bounded region, Theory of Probability & Its Applications 6.3 (1961), 264-274.

[29] V.G. Papanicolaou, The probabilistic solution of the third boundary value problem for second order elliptic equations, Probab. Th. Rel. Fields 87 (1990), 27-77.

[30] Y. Zhou, W. Cai and (Elton) P. Hsu, Local Time of Reflecting Brownian Motion and Probabilistic Representation of the Neumann Problem, Preprint, 2015.

[31] R.P. Feynman, Space-time approach to nonrelativistic quantum mechanics, Rev. Mod. Phys. 20 (1948), 367-387.

[32] M. Kac, On distributions of certain Wiener functionals, Trans. Am. Math. Soc. 65 (1949): 1-13.

[33] M. Kac, On some connections between probability theory and differential and integral equations, in: Proc. 2nd Berkeley Symp. Math. Stat. and Prob. 65 (1951): 189-215.

[34] J.E. Souza de Cursi, Numerical methods for linear boundary value problems based on Feynman-Kac representations, Mathematics and computers in simulation, Vol. 36, No. 1, 1-16, 1994.

[35] A. Lejay and S. Maire, New Monte Carlo schemes for simulating diffusions in discontinuous media, Journal of computational and applied mathematics 245 (2013): 97-116.

[36] H. Tanaka, Stochastic differential equations with reflecting boundary condition in convex regions, Hiroshima Mathematical Journal 9.1 (1979), 163-177.

[37] P.L. Lions and A.S. Sznitman, Stochastic differential equations with reflecting boundary conditions, Communications on Pure and Applied Mathematics 37.4 (1984), 511-537.

[38] J.F. Douglas, Integral equation approach to condensed matter relaxation, Journal of Physics: Condensed Matter 11.10A (1999), A329.

[39] M. Freidlin, Functional Integration and Partial Differential Equations, Princeton University Press, 1985.

[40] C.O. Hwang, M. Mascagni, and J. A. Given, A Feynman-Kac path-integral implementation for Poisson's equation using an h-conditioned Green's function, Mathematics and computers in simulation 62.3 (2003), 347-355.

[41] D.J. Audus, A.M. Hassan, E.J. Garboczi and J.F. Douglas, Interplay of particle shape and suspension properties: a study of cube-like particles, Soft matter 11.17 (2015), 3360-3366.

[42] B. Øksendal, Stochastic differential equations, Springer Berlin Heidelberg, 2003.

[43] I. Karatzas and S. E. Shreve, Brownian motion and stochastic calculus, Springer-Verlag New York Inc., 1988.

[44] K. Burdzy, Z. Chen and J. Sylvester, The heat equation and reflected Brownian motion in time-dependent domains, The Annuals of Probability 32. 1B (2004), 775-804.

[45] Lin, Huimin, Huazhong Tang, and Wei Cai, Accuracy and efficiency in computing electrostatic potential for an ion channel model in layered dielectric/electrolyte media, Journal of Computational Physics 259 (2014): 488-512.

[46] Bossy, Mireille, et al, *Probabilistic interpretation and random walk on spheres algorithms for the Poisson-Boltzmann equation in Molecular Dynamics* ESAIM: Mathematical Modelling and Numerical Analysis 44.5 (2010): 997-1048.

[47] Juba, Derek, et al, Acceleration and Parallelization of ZENO/Walk-on-Spheres, Procedia Computer Science 80 (2016): 269-278.

[48] Borcea, Liliana, Electrical impedance tomography, Inverse problems 18.6 (2002): R99.

[49] Caldern, Alberto P., On an inverse boundary value problem, Computational & Applied Mathematics 25.2-3 (2006): 133-138.

[50] Cheney, Margaret, David Isaacson, and Jonathan C. Newell, Electrical impedance tomography, SIAM review 41.1 (1999): 85-101.

[51] Astala, Kari, and Lassi Pivrinta, Caldern's inverse conductivity problem in the plane, Annals of Mathematics (2006): 265-299.

[52] Borsic, Andrea, Brad M. Graham, Andy Adler, and William RB Lionheart, Total variation regularization in electrical impedance tomography, (2007).

[53] Alessandrini, Giovanni, Stable determination of conductivity by boundary measurements, Applicable Analysis 27.1-3 (1988): 153-172.

[54] Santosa F, Vogelius M, A backprojection algorithm for electrical impedance imaging, SIAM Journal on Applied Mathematics, (1990)216-43.

[55] R. Kohn and M. Vogelius, Determining conductivity by boundary measurements, Comm. Pure Appl. Math., 37 (1984), pp. 113-123.

[56] J. Sylvester and G. Uhlmann, A uniqueness theorem for an inverse boundary value problem in electrical prospection, Comm. Pure Appl. Math., 39 (1986), pp. 91-112

[57] Kaipio, Jari P., et al, Statistical inversion and Monte Carlo sampling methods in electrical impedance tomography, Inverse problems 16.5 (2000): 1487.

[58] Somersalo, Erkki, Margaret Cheney, and David Isaacson, Existence and uniqueness for electrode models for electric current computed tomography, SIAM Journal on Applied Mathematics 52.4 (1992): 1023-1040.

[59] Vauhkonen, Marko, et al. "Tikhonov regularization and prior information in electrical impedance tomography." IEEE transactions on medical imaging 17.2 (1998): 285-293.

[60] D.C. Barber and B.H. Brown, Applied potential tomography, J. Phys. E. Sci. Instrum., 17 (1984), pp. 723-733.

[61] D. Isaacson and M. Cheney, Effects of measurement precision and

nite numbers of electrodes on linear impedance imaging algorithms, SIAM J. Appl. Math., 51 (1991), pp. 1705-1731.

[62] Maire, Sylvain, and Martin Simon, A partially reflecting random walk on spheres algorithm for electrical impedance tomography, Journal of Computational Physics 303 (2015): 413-430.

[63] Russell M. Brown, Global Uniqueness in the Impedance-Imaging Problem for Less Reg- ular Conductivities, SIAM Journal on Mathematical Analysis 27 (1996), no. 4, 1049.

[64] Haberman, Boaz, and Daniel Tataru. "Uniqueness in Calderns problem with Lipschitz conductivities." Duke Mathematical Journal 162.3 (2013): 497-516.

[65] Audus, Debra J., et al, Interplay of particle shape and suspension properties: a study of cube-like particles, Soft matter 11.17 (2015): 3360-3366.

[66] Cheney, Margaret, David Isaacson, and Jonathan C. Newell., Electrical impedance tomography, SIAM review 41, no. 1 (1999): 85-101.

[67] Juba, Derek, Walid Keyrouz, Michael Mascagni, and Mary Brady, Acceleration and Parallelization of ZENO/Walk-on-Spheres, Procedia Computer Science 80 (2016): 269-278.

Publications

[1] Y. Zhou, W. Cai and (Elton) P. Hsu, Computation of Local Time of ReectingBrownian Motion and ProbabilisticRepresentation of the Neumann Problem, Commun. Math. Sci., Vol. 14(2016), No. 185.

[2] Zhou, Yijing, and Wei Cai, Numerical Solution of the Robin Problem of Laplace Equations with a FeynmanKac Formula and Reflecting Brownian Motions, Journal of Scientific Computing (2016): 1-15.